

We are IntechOpen, the world's leading publisher of Open Access books Built by scientists, for scientists

6,900

Open access books available

186,000

International authors and editors

200M

Downloads

Our authors are among the

154

Countries delivered to

TOP 1%

most cited scientists

12.2%

Contributors from top 500 universities



WEB OF SCIENCE™

Selection of our books indexed in the Book Citation Index
in Web of Science™ Core Collection (BKCI)

Interested in publishing with us?
Contact book.department@intechopen.com

Numbers displayed above are based on latest data collected.
For more information visit www.intechopen.com



Solution and Suspension Plasma Spraying of Nanostructure Coatings

P. Fauchais and A. Vardelle

SPCTS, UMR 6638, University of Limoges, European Center of Ceramics, Limoges, France

1. Introduction

The main motivation for coating industrial parts with a different material lies on the following needs: (1) to improve functional performance, (2) to improve the component life by reducing wear due to abrasion, erosion and/or corrosion, (3) to extend the component life by rebuilding the worn part to its original dimensions, and (4) to improve the functionality of a low-cost material by coating it with a high performance but more expensive coating. Coating technologies can be roughly divided into thin- and thick- film technologies. Thin films, with thickness of less than 20 μm can be produced by dry coating processes like Chemical Vapor Deposition (CVD) or Physical Vapor Deposition (PVD); they offer excellent enhancement of surface properties and are for example used in optical and electronic device and cutting tools, *Davis J.R. (2004)*. However, most of these thin-film technologies require a reduced pressure environment and, therefore, are more expensive with a limit on the size and shape of the substrate.

Thick films have a thickness over 20 μm and can be several millimeters thick. They are required when the functional performance depends on the layer thickness, e.g. in thermal barrier coatings, when high erosion and corrosion conditions result in wear and the component life depends on the layer thickness, or when the original dimensions of worn parts have to be restored. Thick film deposition methods include chemical/electro-chemical plating, brazing, weld overlays, and thermal spray. Thermal spray processes, *Davis J.R. (2004)*, are well-established surface treatments aiming at forming a coating by stacking of lamellae resulting from impact, flattening and solidification of impinging molten particles. "Thermal spraying comprises a group of coating processes in which finely divided metallic or non-metallic materials are deposited in a molten or semi-molten condition to form a coating. The coating material may be in the form of powder, ceramic rod, wire or molten materials, *Hermanek, F.J. (2001)*."

A thermal spray system consists of five subsystems:

1. The high energy, high velocity jet generation that includes the torch, power supply, gas supply, and the associated controls;
2. The coating material preparation, i.e. powder manufacturing that controls particle size distribution and morphology, injection by a carrier gas into the high energy gas jet and transformation into a stream of molten droplets;

3. The surrounding atmosphere, i.e. atmospheric air, controlled atmosphere (including humidity control), low pressure, etc.;
4. The substrate material and surface preparation; and
5. Mechanical equipment for controlling the motion of the torch and the substrate relative to each other.

The main driving force for R&D on the manufacture of thick coatings by thermal spraying is their high deposition rate (a few kilograms per hour of feedstock can be processed with torches with a few tens kW power level) at a relatively low and limited operating cost. Thermal spray processes include flame spraying, plasma spraying, wire arc spraying, and plasma transferred arc (PTA) deposition. Plasma spraying is probably the most versatile of all thermal spray processes because there are few limitations on materials that can be sprayed, and few limitations on the material, size and shape of the substrate, *Fauchais P. (2004)*. Coatings are used in numerous industrial fields, as aeronautical and land-based turbine industries (e.g., thermal barrier coatings, abradable seals, etc.), biomedical industry (e.g., hydroxyapatite bio-integrable coatings onto orthoprotheses) and paper industry (e.g., abrasion wear resistant and corrosion resistant coatings) *Davis J.R. (2004)*. Coatings are formed by stacking of lamellae resulting from impact, flattening and solidification of impinging molten particles. They are characterized by a highly anisotropic lamellar structure. Moreover, stacking defects generate specific interlamellar features within the structure, mainly voids, which can be, or not, connected to the upper surface of the deposit (i.e., connected and open voids, respectively).

Conventional thermal spray processes use powders with particle size ranging from 10 to 100 μm . They result in coatings that mainly present micrometer-sized features, as the lamellae formed by the impact of the particles onto the substrate are a few μm thick with diameter from a few tens to a few hundreds of micrometers. The interest for developing and studying thermal-sprayed coatings that exhibit nanometer-size features and not micrometer-sized features has been important over the past 30 years and very important the last ten years. This interest comes from the enhanced properties of nanometer-sized coatings as compared to micrometer-sized ones. Reducing the structure scale down to nanometer allows, *Gell (1995)*, increasing strength, improving toughness and coefficient of thermal expansion while reducing apparent density, elastic modulus, and apparent thermal conductivity, among other improvements. One of the major drawbacks in processing nanometer-sized particles by thermal spraying is the difficulty in injecting them in the core of the high enthalpy flow, since the particle injection force has to be of the same order as that imparted by the gas flow: $S \cdot \rho_g \cdot v_g^2$, where S is the cross section of the injected particle, ρ_g the specific mass of the plasma and v_g the plasma velocity. Of course the last two terms vary along the particle trajectory in the plasma jet. The force of the injected particle is proportional to its mass (depending on the cube of its diameter) and the velocity of the carrier gas flow, which must be substantially increased as soon as the particle size decreases. However, the carrier gas flow rate disrupts the plasma jet as soon as its mass flow rate is over 1/5 of that of the plasma-forming gas. Thus, it is not practically possible to inject particles with sizes below 5-10 μm .

Four possibilities exist to circumvent this drawback (see the reviews of *Fauchais et al (2008) and (2011)*, *Pawlowski (2008)* and *Viswanathan et al (2006)*). They consist of spraying:

1. Micrometer-sized agglomerates made of nanometer-sized particles that are injected using conventional injection route based on carrier gas. The operating spray parameters must, then, be adjusted in such a way that the molten front within such agglomerated particles progresses slower compared to the one in fully dense particles of same diameters. Upon solidification, the molten fraction of particles (for example the smallest particles or the outer shell of larger particles made of a single element) generates micrometer-sized zones in the coating ensuring its cohesion while the unmolten fraction of particles (inner core) keep their nanometer-sized structure. Such a coating architecture is usually called as "bimodal".
2. Complex alloys (5 to 10 components) that have low critical cooling rates for metallic glass formation result in the formation of amorphous coatings when thermally deposited. The amorphous coatings, when heated after spraying, to above their crystallization temperature, are devitrified. Since the diffusion rate in the solid state is very low at the transformation temperature (typically 0.4–0.7 T_m for iron alloys, T_m being the melting temperature), nanometer-scale microstructures are formed.
3. A suspension of nanometer-sized particles, with the carrier gas replaced by a liquid ("Suspension Thermal Spraying": STP). The nanometer-sized particles are dispersed into the liquid phase by means of dispersants: the suspension is then injected either as a liquid stream or as drops after nebulization. Depending upon the injection and plasma jet conditions, the liquid stream or droplets are fragmented due to flow shear forces and vaporized.
4. Precursors in solution that will form in-flight nanometer-sized particles ("Solution Precursor Thermal Spraying": SPTS). This significantly limits the safety issues associated with handling of nanometer-sized particles (e.g. see the very complete review by Singh et al. (2009)) and avoids most of the drawbacks associated with suspension stabilization, in particular when dissimilar materials (e.g., metallic alloys and oxides) are mixed together.

The following sections discuss successively: plasma torches and plasma jets used for suspension or solution spraying, interaction of the plasma jet with liquids, the preparation of suspensions and solutions, the nanometer structured coatings obtained and, their characterization and finally potential applications.

2. Plasma torches used for suspension or solution spraying

2.1 Conventional direct current plasma torches

Most spraying processes are carried out in air at atmospheric pressure, except for radio frequency r.f spraying. A conventional d.c. plasma torch (more than 90% of industrial torches are operated at power levels below 50 kW) with a stick type cathode is shown schematically in Figure 1a *Fauchais (2004)*. The cathode is made of thoriated (2 wt %) tungsten and the anode-nozzle of high purity oxygen-free copper encasing a cylindrical insert of sintered tungsten with internal diameter (i.d.) between 5 and 8-mm. The arc column (3 in Figure 1a) develops between the conical cathode tip (Θ in Figure 1a) pumping part of the plasma-forming gas (1 in Figure 1a), the other part flowing along the anode wall (cold boundary layer 2 in Figure 1a). The most commonly used plasma gases are: Ar, Ar-He, Ar-H₂, N₂, N₂-H₂, but more complex mixtures such as Ar-He-H₂ are also used. Ar and N₂ are

mostly used for their mass, while the secondary gases (He and H₂) are used for their thermal properties: For example, 25 vol. % of H₂ in Ar increases the mean thermal conductivity of Ar by a factor 8 at 4000 K, *Boulos et al (1994)*. In comparison to H₂, He increases the thermal conductivity of the plasma and, its high viscosity up to about 14000 K delays the mixing of the surrounding air with the plasma jet.

The arc attachment to the anode wall, through the connecting column (4 in Figure 1a), continuously fluctuates in length and position. This is due to the movements induced by the drag force of the gas flowing in the cold boundary layer (2 in Figure 1a), the arc chamber pressure fluctuations, the Helmholtz oscillations in the space upstream of the arc, *Coudert et al (2007)*, and the magneto-hydrodynamic forces, all of which resulting in upstream and downstream short circuits. The corresponding transient voltage, which depends on the cold boundary layer thickness in the arc attachment area, exhibits a restriking (saw tooth shape), take-over (regular periodic variation) or mixed mode, and its value can reach $\pm 75\%$ of the time-averaged voltage. The restriking mode is the most probable with plasma forming gases that contain diatomic gases, while the take-over mode mainly occurs with monoatomic gases, these phenomena being drastically enhanced by the Helmholtz oscillations.

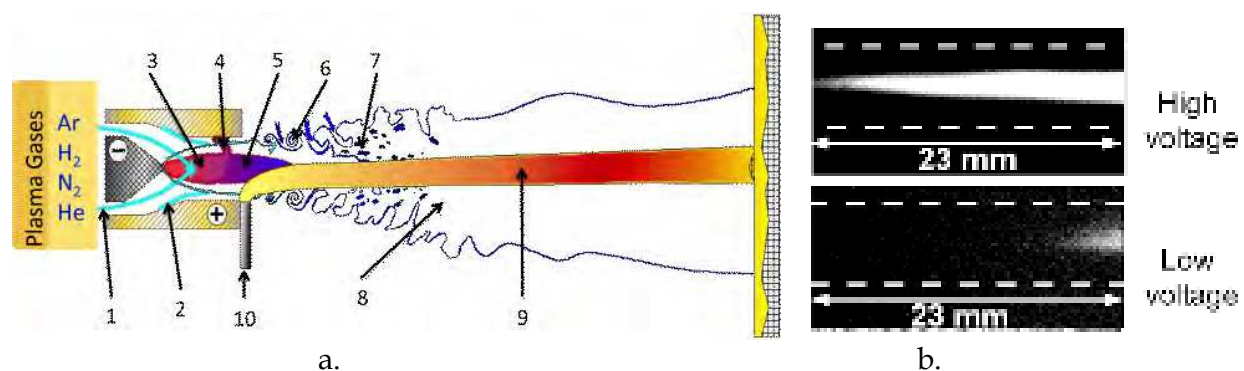


Fig. 1. (a.) schematic of a conventional dc arc spray torch with: \ominus – stick type thoriated tungsten cathode, \oplus – anode; nozzle 1 – the plasma forming gas injection, 2 – the cold boundary layer at the anode wall, 3 – the arc column, 4 – the connecting arc column, 5 – the plasma jet exiting the nozzle, 6 – the large scale eddies, 7 – the surrounding atmosphere bubbles entrained by the engulfment process, 8 – the plasma plume, 9 – particles jet, 10 – injector. (b.) plasma jet pictures taken with a shutter time of 10^{-4} s at maximum and minimum voltages: Ar-H₂ (45-15 slm) plasma produced with a PTF4 torch, anode-nozzle internal diameter $d = 6$ mm, arc current $I = 600$ A.

The arc root fluctuations help to keep the anode integrity because the heat fluxes at the arc root can be as high as 10^9 - 10^{10} W.m⁻² thus limiting the residence time of the arc root to about 150 μ s. Voltage fluctuations are characterized by the ratio $\Delta V/V_m$ (ΔV being the fluctuation amplitude and V_m the average voltage) that can vary from 0.25 (in the best conditions of the takeover mode) to 1.5 (in the worst conditions of the restriking mode). Correspondingly, the power dissipated in the arc, and thus the enthalpy, fluctuates with arc voltage (the torch being supplied by a constant current source) resulting in plasma jets continuously fluctuating in length and position (Figure 1a) at frequencies ranging between 2000 and 8000 Hz, depending on the cold boundary layer thickness *Fauchais (2004)*. An example is given in Fig. 1b representing pictures of an Ar-H₂ (25 vol. %) d.c. plasma jet taken at the highest (80

V) and lowest (40 V) voltages, respectively. As the plasma enthalpy fluctuates, the momentum density of the plasma jet ($\rho_g \times v_g^2$) at a given location in the jet also varies substantially with time. For $\Delta V/V_m=1$, the plasma flow average specific mass, ρ_g (depending on T), varies by less than 30%, while v can vary by a factor of up to 2 or 3. The injection force imparted by the carrier gas to a conventional particle (i.e. a few tens of micrometers in diameter), cannot follow the arc root fluctuations that are in the few kilohertz range. Therefore, the average particle trajectory fluctuates accordingly and, the temperature and velocity of the particles fluctuate at the same frequency as that of the arc root *Bisson et al (2003)*. The effect on the micrometer-sized coating morphologies can be rather important: i.e, less dense and more porous coatings are obtained with highly fluctuating plasma jets than those obtained with more stable plasma jets with the same enthalpy.

The effects of these fluctuations are even more drastic when the feedstock material injected in the plasma jet is in liquid form (suspension or solution) (see section 3). Therefore, Ar-He mixtures, which bring about lower fluctuations are often used to spray liquid feedstock, in spite of the fact that the power level is lower than that reached with diatomic gases *Fauchais et al (2011)*. Most of the temperature and velocity measurements of plasma jets have been performed in time ranges that integrate fluctuations. Under these conditions, typical plasma jet temperatures at the torch nozzle exit are between 14000 and 8000 K, irrespective of the plasma-forming gases and anode-nozzle internal diameter, while jet velocities vary with these two parameters between 800 and 2200 m s⁻¹, i.e. sub-sonic velocities at these temperatures and atmospheric pressure.

2.2 Other direct current plasma torches

To spray liquid suspensions or solutions, two other types of d.c. torches were developed in the nineties:

- Plasma torches with three cathodes insulated between them and supplied by independent power sources as the Triplex® system from Sulzer-Metco. The electrical energy is distributed through three parallel arcs striking at a single anode preceded by insulating rings (Figure 2). The internal diameter (i.d.) of the nozzle is between 6 and 8 mm. The generation of arcs that are longer than in conventional dc plasma torches makes it possible to reduce significantly (4 to 5 times) the percentage of voltage fluctuations of these torches compared to conventional dc plasma torches. Indeed if the voltage is more important with the long arc the voltage fluctuations at the anode are similar to those obtained with a conventional d.c. plasma torch, or even smaller with the more limited anode attachment. Figure 2(b) shows an Ar-He plasma jet produced by the Triplex II torch and illustrates its stability (compare with Figure 1(b)). Moreover, the threefold symmetry with three feedstock injectors can be aligned towards the warmest or coldest parts of the plasma jet to enable the optimization of the injection of the feedstock material.
- Plasma torches composed of three cathodes and three anodes operated by three power supplies (total power ranging from 50 to 150kW), such as Axial III® from Mettech. The feedstock material is injected axially between the three plasma jets converging within an interchangeable plasma nozzle. Hence, the particle residence time in the hot zones can be drastically improved.

2.3 Radio frequency plasma torches

Radio frequency torches used for spraying have internal diameters of 35 to 60 mm and power levels below 100 kW. The main differences with d.c. torches are in the torch i.d., resulting in flow velocities below 100 m.s^{-1} and in the axial injection of particles. As can be seen in Figure 3, the injector is positioned almost at the middle of the coil. As the coupling between the coil and the plasma occurs in a ring close to the wall, the gas close to the torch axis is heated only by convection-conduction, and the water-cooled injector can be positioned axially with no coupling to the coil. In the spray RF plasma torches supplied by TECKNA (only industrial supplier of RF plasma spray torches), a ceramic tube with a higher thermal conductivity replaces the quartz tube generally used in RF plasma torches.

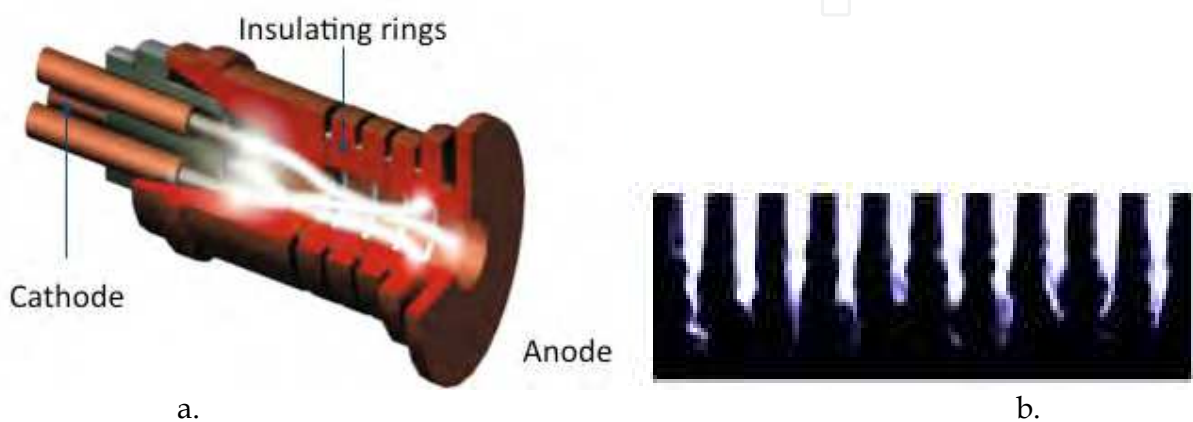


Fig. 2. (a) Schematic view of Triplex® Plasma torch, (b) Pictures of the plasma jet: Aperture time: $1.5 \mu\text{s}$, time between images: $130 \mu\text{s}$.

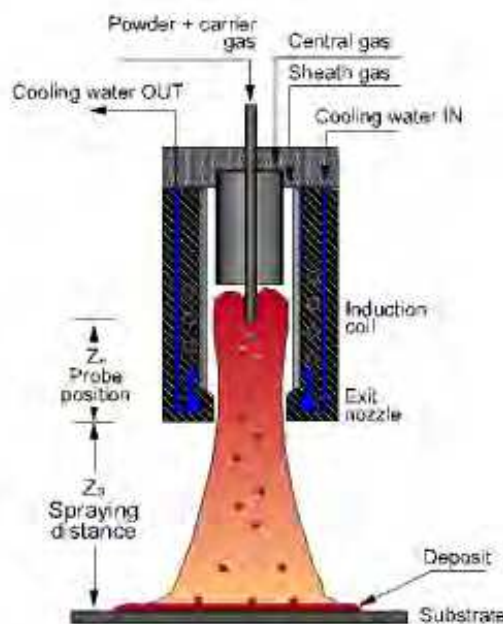


Fig. 3. Principle of radio frequency plasma spraying Fauchais (2004).

The coil is inserted in the torch body and it allows a perfect alignment and a smaller separation between the coil and the discharge and, thus, a better coupling.

The combination of these elements with a careful aerodynamic design of gas injectors and laminated high-velocity water-cooling allows reliable functioning at high power density. Spray torches with power levels up to 100 kW generally operate at 3.6 MHz. As the gas velocity is nearly inversely proportional to the square of the torch i.d, that is the plasma gas velocity is below 100 m.s^{-1} , corresponding to particle velocities below 60 m s^{-1} and correspondingly high residence times (in the tens of milliseconds range). These conditions allow for the melting of metallic particles up to $200 \mu\text{m}$ with argon despite its low thermal conductivity. Using argon as the plasma forming gas allows for easy coupling at reasonable power levels. However, the sheath gas can also be pure oxygen allowing, for example, to spray materials that are very sensitive to oxygen losses such as perovskites.

3. Plasma–liquid interaction

3.1 Measurements and modeling

The visualization of the interaction between the liquid feedstock and plasma jet is necessary for better understanding the involved phenomena. *Etchart-Salas et al (2007)* were the first to propose a solution by using the fast-shutter camera of a Spray Watch detector from Oseir® coupled with a laser (808 nm wavelength) sheet flash. The image recording (Figure 4a) was triggered when the transient voltage reached a certain threshold. According to the image size and the number of pixels (600×600), one pixel represented an area of about $30 \mu\text{m}^2$. It is thus impossible with such a device to visualize droplets of sizes below $5\text{--}6 \mu\text{m}$ in diameter. To obtain more information on the plasma jet-liquid stream interactions, 10 images taken under the same conditions (in about 1 s) were superimposed after having eliminated the luminosity of the plasma jet. The resulting final image allowed determining two characteristic angles of the liquid stream penetration in the plasma jet: the dispersion angle (θ) and the deviation angle (α), as illustrated in Figure 4b.

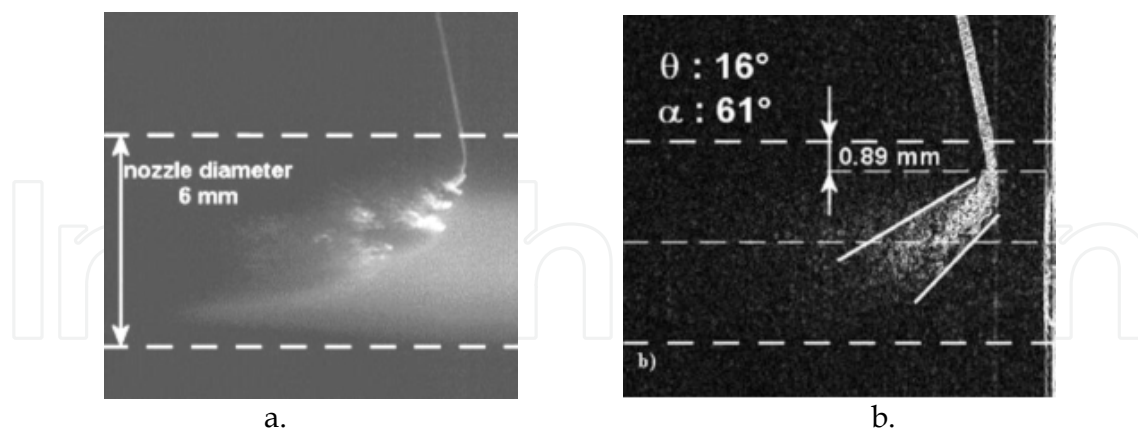


Fig. 4. (a) Picture taken with a laser flash of an ethanol suspension mechanically injected at a velocity of 33.5 m.s^{-1} in an Ar-He (30-30 slm) plasma jet (700 A, 40 V, anode-nozzle i.d. 6mm), (b) Image obtained by superposing ten successive images in the same conditions, *Etchart-Salas (2007)*.

More sophisticated devices, e.g., using a shadowgraph technique coupled with particle image velocimetry (PIV), also allowed observing the drops within the plasma jet and measuring their number, size and velocity. A double-pulsed Nd:YAG laser (532 nm

wavelength with 8 ns pulse duration) backlight illuminated the liquid material. The detection system consisted of two charge-coupled device (CCD) cameras with 1376x1040 pixels and 12 bits resolution. A programmable hardware-timing unit controlled the synchronization of the laser with the cameras *Fauchais and Vardelle (2011)*. With this system, it was possible to observe the behavior of droplets down to about 3-5 μm , and to measure their velocity and diameter distributions in a relatively small volume ($2.5 \times 2 \times 1.5 \text{ mm}^3$). This technique is very useful under plasma spray conditions to validate model predictions and observe the effect of operating parameter change. However results have to be cautiously interpreted and need to be coupled with pyrometer measurements.

The effect of liquid injection onto the plasma jet temperature can be performed by emission spectroscopy, as shown by *Fazilleau et al (2006)*. However the axial symmetry of the plasma jet is destroyed in the injection zone and recovered only when the liquid has been fragmented and vaporized, thus tomography is mandatory, *Landes (2006)*.

Caruyer et al (2010) have developed the numerical simulation of the interaction between a liquid jet and a plasma flow. They described the dispersion of liquid in order to understand the effect of injection conditions on the surface coating quality. They proposed an original model for dealing with three-dimensional interactions between the d.c. plasma flow and a liquid phase with "volume of fluid" (VOF) method. A compressible model, capable of representing incompressible two-phase flows as well as compressible motions, was used. The first comparisons of predictions with experimental shadowgraphy data showed fair agreement during the first moments of the injection.

3.2 Liquid injection

Two main techniques are used: atomization or mechanical injection.

3.2.1 Spray atomization

This method has been used for suspensions and solutions, *Rampon et al (2008)*. Very often, co-axial atomization is used. It consists of injecting a low velocity liquid inside a nozzle where it is fragmented by a gas (mostly Ar because of its high mass density) expanding within the body of the nozzle, *Filkova I. and P. Cedik (1984)*. For liquids of viscosity between a few tenths to a few tens of mPa.s, their break-up into drops depends on the Weber number, which expresses the competitive effects of the force exerted by the flow on the liquid and surface tension forces. This means that for a liquid with a given surface tension atomization depends on both gas velocity and specific mass. Atomization also depends, but to lesser extent, on the Ohnesorge number including the effect of liquid viscosity. Weber, We , and Ohnesorge, Z , dimensionless numbers are defined as follows:

$$We = \rho_g \cdot u_r^2 \cdot d_l / \sigma_l \qquad Z = \mu_l / \sqrt{\rho_l \cdot d_l \cdot \sigma_l}$$

where ρ_g is the gas mass density, μ_l the liquid viscosity, u_r the relative velocity between the gas and the liquid, d_l the diameter of the droplet and σ_l the surface tension of the liquid phase.

However, if the viscosity is too high ($> 0.8 \text{ mPa.s}$), difficulties with feeding the liquid may appear. Measurements showed that atomization was affected by the following parameters:

the relative velocity between the liquid and the gas, the ratio of the gas to liquid volume feed rates, called RGS (generally over 100), or the gas-to-liquid mass ratio, called ALR (less than 1), the nozzle design, and the properties of the liquid (density, surface tension, dynamic viscosity). For example, depending on the Ar atomizing flow rate, the mean droplet diameters of alcohol vary between 18 and 110 μm . Also, for the same injection parameters, shifting from ethanol ($\sigma_{\text{eth}} = 22 \cdot 10^{-3} \text{ N/m}$ at 293 K) to water ($\sigma_{\text{w}} = 72 \cdot 10^{-3} \text{ N/m}$) modifies the mean diameter from 70 to 200 μm . Increasing the atomizing gas constricts the droplet jet and also perturbs the plasma jet. Similar results have been obtained when considering the influence of RGS, the droplet size is diminished with the increase of RGS. Quadrupling the RGS leads to a decrease in the droplet size by a factor of ten and allows obtaining a narrower Gaussian curve. It is also interesting to note that the weight percentage of solid in the suspension broadens the particle size distribution. For more details the reader is referred to the book of *Lefebvre (1989)*. For example, *Jordan et al (2008)*, have used three different types of atomizers to spray solutions: (1) a narrow angle hydraulic atomizing fan nozzle, (2) an air cap transverse air blast atomizing nozzle with a relatively large spray angle, and (3) a home made capillary atomizer with a liquid exiting one capillary and an air atomizing jet at 90 degrees to the liquid discharge used as a transverse jet atomizer. Of course the drop size distribution is the broadest with the air cap atomizer and the narrowest for the capillary atomizer with which the best coatings are achieved.

3.2.2 Mechanical injection

Two main techniques are possible: either to have the liquid in a pressurized reservoir from where it is forced through a nozzle of given i.d., or to add to the previous set-up a magnetostrictive rod at the back side of the nozzle which superimposes pressure pulses at variable frequencies (up to a few tens of kHz).

For example the first device developed at the SPCTSLaboratory of the University of Limoges, France, *Etchart-Salas (2004)*, consisted of four tanks in which different suspensions and one solvent were stored. Any reservoir or both of them could be connected to an injector consisting of a stainless steel tube with a laser-machined nozzle with a calibrated injection hole. A hole of diameter d_i produced a liquid jet with a velocity v_i (m/s) linked to the incompressible liquid mass flow rate (kg/s) by the following equations:

$$m_l^0 = \rho_l \cdot v_l \cdot S_i \quad \text{and} \quad \Delta p = f \cdot \rho_l \cdot v_l^2 / 2$$

where ρ_l is the liquid specific mass ($\text{kg} \cdot \text{m}^{-3}$) and S_i the cross sectional area of the nozzle hole (m^2). Assuming that the liquid is non-viscous and ideal, v_i depends on the pressure drop Δp between the tank and surrounding atmosphere through the Bernoulli equation where f is a correction factor (0.6 to 0.9) for friction and viscous dissipation. For example with an injector i.d. of 150 μm , the tank pressure was varied between 0.2 and 0.6 MPa to achieve injection velocities between 22 and 34 $\text{m} \cdot \text{s}^{-1}$. To achieve the same injection velocity with a d_i of 50 μm as the velocity obtained at 0.5 MPa with $d_i = 150 \mu\text{m}$, the pressure should be multiplied by 81 and so reached 40.5 MPa requiring adapted equipment and special precautions!. The liquid exiting the nozzle, observed with a CCD camera, flows as a liquid jet, with a diameter between 1.2 and 1.5 d_i depending on the tank pressure and nozzle shape. After a length of about 100-150 times d_i , Rayleigh-Taylor instabilities lead to fragmentation of the jet into drops with a diameter of about 1.3-1.6 times that of the jet. Thus, depending on the position

of the injector exit relative to the plasma jet (radial injection), either a liquid jet or droplets are injected in the plasma jet.

Blazdell and Kuroda (2000) used a continuous ink jet printer, which allowed uniformly spaced droplets to be produced by superimposing a periodic disturbance on a high-velocity ink stream. They used a nozzle 50 μm in i.d. (d_i) and a frequency f of 74 MHz producing 64,000 droplets/s. *Oberste-Berghaus et al. (2005)* have used a similar set-up with a magnetostrictive drive rod (Etrema AU-010, Ames, Iowa) at the backside of the nozzle, working up to 30 kHz. They produced 400- μm drops with 10- μs delay between each and with a velocity of 20 m/s.

3.2.3 Liquid penetration into the plasma flow

In conventional particle spraying where the injection force of the particle is nearly that imparted to it by the plasma jet, the optimum particle trajectory is achieved (see Introduction). For liquid jet or drops injection, when they penetrate within the plasma jet they are progressively fragmented and their volume and apparent surface become smaller. Accordingly, the mass of the drops as well as the force imparted to them by the gas jet is reduced. Thus, drop penetration ceases rapidly, and the condition for good penetration implies that $\rho_l v_l^2 \gg \rho_g v_g^2$. For example, considering a suspension of zirconia in ethanol injected into an Ar-He d.c. plasma jet, a better penetration of the liquid jet within the plasma jet core is achieved when its velocity is 33.5 m.s⁻¹ instead of 27 m.s⁻¹. In the first case, the liquid jet momentum density is 0.96 MPa against 0.02 MPa for the mean value of that of the plasma jet (with a 27 m.s⁻¹ injection velocity the liquid jet momentum is still 0.6 MPa).

3.2.4 Drops or jet fragmentation and/or vaporization

Upon penetration in the plasma jet, drops or liquid jet are submitted (i) to a strong shear stress due to the plasma flow, which, under conditions described below, fragment them into smaller droplets, and (ii) to a very high heat flux that vaporizes the liquid. Thus, a very important point is the value of the fragmentation time, t_f , relatively to the vaporization time, t_v , in order to see if the two phenomena can be separated. One approach is that of complex models, such as that of *Caruyer et al (2010)*. They considered (i) 3-D transient or stationary description of the turbulent plasma flow and its mixing with the ambient atmosphere, (ii) a suitable description of the liquid feedstock injection as jet, drops or droplets into the plasma jet and (iii) an accurate description of the possible mechanisms that control the treatment of the liquid material in the plasma flow (i.e. mechanical break-up, thermal break-up, coalescence). The fragmentation undergone by drops or jets has been extensively studied for cold gas impacting orthogonally a liquid jet *Lee and Reitz (2001)*. These results have been considered to be a valid first approximation for the interaction of hot gases or plasmas and a liquid even though thermal effects are not considered. However, if results established for cold gases are acceptable in understanding the implied phenomena, experiments should be implemented with hot gases to validate them. The fragmentation depends upon the dimensionless Weber number, We , (section 3.2.1) and according to its value different regimes can be considered:

- for $12 < We < 100$, the fragmentation is named 'bag break-up': it corresponds to the deformation of the drop as a bag-like structure that is stretched and swept off in the flow direction;

- for $100 < We < 350$, the fragmentation is named 'stripping break-up' : thin sheets of liquid are drawn from the periphery of the deforming droplets;
- for $We > 350$, the fragmentation is named 'catastrophic break-up' and corresponds to a multistage breaking process.

The main question is when fragmentation occurs? Indeed, the We number increases with the relative velocity between the drop and the jet, u_r , and with the drop size. The different limit values of this number can be slightly modified according to the Ohnesorge number.

- For r.f. plasmas where gas velocities are below 100 m.s^{-1} , where axially injected drops have sizes over $20\text{-}30 \mu\text{m}$, fragmentation is highly improbable and the main phenomena are the liquid vaporization followed by the heat treatments of the particles contained in the liquid (suspension) or formed in flight (solutions).
- For d.c. plasma jets with radial injection of the liquid in the plasma jet the story is quite different. $We > 12$, except if the injected drops are less than a few tens of micrometers, and the fragmentation process starts in the plasma jet fringes before drops have reached the hot plasma core, as illustrated in Figure 5a from *Etchart-Salas (2007)*. As explained in section 5, the main problem when fragmentation starts in the d.c. plasma jet fringes is that the fragmented droplets are nevertheless vaporized and their content heated enough to stick onto the coating under formation and create stacking defects. Of course when the atomized liquid exhibit rather broad distributions of drop size and velocity, drop penetration within the plasma jet is poorly controlled, as shown in Figure 5b and creates stacking defects within coating.



Fig. 5. (a) Example of fragmentation of an ethanol jet, about $300 \mu\text{m}$ in diameter, starting in the fringes of a d.c. plasma jet (Ar-He: 30-30 slm, 700 A, 40 V, Anode-nozzle i.d. 6 mm) *Etchart-Salas et al (2007)*, (b) Interaction of an Ar-H₂ plasma jet with atomized ethanol drops *Fazilleau et al (2006)*.

A very important point is the value of the fragmentation time t_f relative to that of vaporization time t_v . The fragmentation time can be roughly calculated by assuming that atomization is completed when the liquid surface tension force is equal to the drag force of the plasma jet resulting in a minimum droplet diameter d_m . *Fazilleau et al (2006)* studied the fragmentation of ethanol drops along their mean trajectory in an Ar-H₂ d.c. plasma jet (operating parameters: Ar-H₂ 45-15 slm, 500A, $V_m = 65 \text{ V}$, anode-nozzle i.d. 6mm). For the calculation of the fragmentation and evaporation times, they considered the plasma temperatures and velocities "seen" by so-called mother drops of various diameters and

resulting droplets along their trajectories. They also took into account the buffer effect due to the vaporization of the liquid phase and the Knudsen effect. The results are summarized in Figure 6. It has to be kept in mind that these calculations did not consider the plasma jet cooling resulting from the vaporization of the liquid phase and, thus, the drop diameter decrease along the plasma jet radius was probably overestimated. Nevertheless it can be readily seen that, in the plasma jet fringes, the drop diameter starts to be reduced due to fragmentation and the resulting droplets very rapidly decrease in size because of vaporization. Fragmentation and vaporization times differed by at least two orders of magnitude whatever the considered diameter of the mother drop. It is also important to note that the vaporization time of a drop 300 μm in diameter is about 4 orders of magnitude longer than that of a drop of 3 μm , which is 100 times smaller. The fast ($< 1 \mu\text{s}$) fragmentation of drops followed by the fast ($\sim 1 \mu\text{s}$) vaporization of resulting droplets explains the sequence of successive events in an Ar-H₂ plasma jet upon water drop penetration *Fazilleau et al (2006)*. The plasma jet is at first disrupted into two parts distributed on both sides of the plane defined by the torch centerline axis and the injector axis. Then, the axial symmetry is restored 15 mm downstream of the nozzle exit. Once drops are fragmented into much smaller droplets, they are vaporized very fast and the liquid phase vapor is rapidly transformed into plasma. Assuming no evaporation, the predicted residence time of a 2 μm water droplet located on torch centerline at nozzle exit is of the order of ten microseconds for the first 15 mm of trajectory. These characteristic times clearly demonstrate that droplets are fully vaporized in the hot core of the plasma jet as about 1 μs is sufficient to vaporize a droplet 2 μm in diameter, and the water vapor is transformed into plasma.

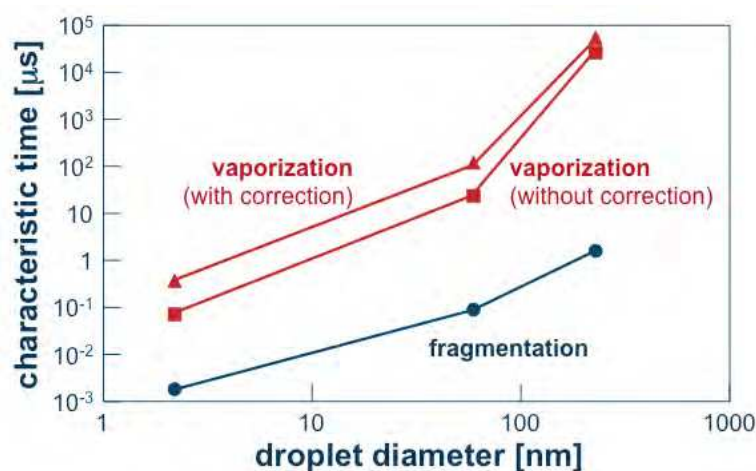


Fig. 6. Variation of fragmentation and vaporization times of ethanol drops with droplet diameter without and with the correction that takes into account the buffer effect of the vapor cloud around droplets for a stationary ($V = 65 \text{ V}$, $I = 600 \text{ A}$, nozzle i.d. 6 mm) Ar-H₂ plasma jet *Fazilleau et al (2006)*.

3.2.5 Effect of plasma jet fluctuations

Arc root fluctuations have a more important negative effect on liquid injection than they have on powder particle injection. For example with an Ar-H₂ plasma jet (Ar-H₂ 45-15 slm, 500 A, $V_m = 65 \text{ V}$, anode-nozzle i.d. 6mm) with arc operating in the restrike mode, the arc

voltage varies between 40 and 80 V, resulting in high variations of the plasma jet length, as illustrated in Fig. 1b. A difference of 40 V in arc voltage corresponds to a variation in the predicted mean velocities of gas of about 800 m.s^{-1} , resulting approximately in a gas momentum density variation ($\rho_g.v_g^2$) of 320%! These variations bring about different penetrations of the suspension stream in the plasma flow, as illustrated in Figure 7. The liquid jet dispersion angle (θ) for an arc voltage of 40 V is about 64° when it is about 33° for an arc voltage of 80 V while the deviation angle (α) is almost constant. Therefore, Ar-He plasma gas that exhibit lower arc voltage fluctuations are often preferred to Ar-H₂ plasma gas, even if the arc power levels are lower, except with the Triplex® torch.

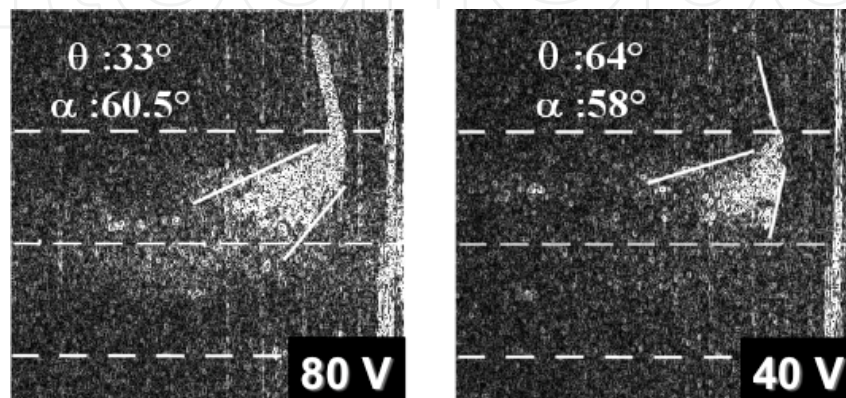


Fig. 7. Plasma jet-suspension stream interactions for arc voltage of (a) 80 V and (b) 40 V (suspension stream injection velocity of 26.6 m.s^{-1} , distance between the injector tip and the torch centerline axis of 20 mm, other working parameters depicted above) *Etchart-Salas et al (2007)*.

3.2.6 Effect of liquid injection velocity

To counteract the strong decrease in drop sizes when they penetrate the plasma jet because of break-up mechanisms, the liquid injection velocity must be increased. For example with the Ar-He plasma jet presented in Figure 4b the liquid injected at 33.5 m.s^{-1} travels 0.89 mm in the jet fringes without fragmentation and goes beyond the torch axis while when it is injected at 27 m.s^{-1} , fragmentation starts after 0.58 mm trajectory in the plasma jet fringes and the visible part of the fragmented jet hardly reaches the torch axis.

3.2.7 Effect of liquid vaporization

The liquid vaporization and then the transformation of the vapor into plasma consume energy and cool down the plasma jet. For example when a water jet with a mass flow rate of $3.6 \times 10^{-4} \text{ kg/s}$ (typical flow rate for liquid injection) is injected in an Ar-H₂ (25vol.%) plasma jet with a mass flow rate of $1.36 \times 10^{-4} \text{ kg/s}$ and a mass enthalpy of 32 MJ.kg^{-1} the latter decreases by almost 9 MJ.kg^{-1} , *Fazilleau et al (2006)*. Correlatively the plasma jet core length where temperature is over 8000 K is reduced by 25%. Spectroscopic measurements showed that about 15 mm downstream of the liquid injection the symmetry of the jet, cut into two parts at the injection location, was restored: a large part of the liquid was evaporated and transformed into plasma, and the remaining droplets were uniformly distributed within the plasma jet core. Of course liquids with lower vaporization energies as ethanol cool down

less the plasma. However, generally when the vaporization energy decreases, the surface tension also decreases favoring liquid fragmentation in the plasma jet fringes.

4. Suspensions and solutions preparation

4.1 Suspension preparation

4.1.1 Slurry route

The easiest way to prepare a suspension is to make slurry with particles and liquid phase, particle sizes varying from a few tens of nanometers to a few micrometers. The most used liquid phases are ethanol, water or a mixture of both, *Fauchais (2007)*. After stirring, the suspension stability can be tested by a sedimentation test. Typical values of slurry stability are a few tens of minutes up to a few hours, and the stability increases with the mass load, *Rampon et al (2008)*. However, for loads over 15–20 wt.%, solid particles are less melted when they are sprayed. Slurries with TiO_2 , ZrO_2 , Al_2O_3 and $\text{ZrO}_2\text{-Al}_2\text{O}_3$ have been prepared following this route, *Fauchais et al (2011)*. However, it should be noted that nanometer-sized particles of oxides have the tendency to agglomerate or aggregate, even when stirring the suspension. This drawback can be partially or totally overcome by using a suitable dispersant, which adsorbs on the particle surface and allows an effective dispersion of particles by electrostatic, steric or electro steric repulsions. For example, a phosphate ester that aids particle dispersion by a combination of electrostatic and steric repulsion has been used with zirconia particles, *Fazilleau et al (2006)*. The percentage of dispersant must be adjusted in such a way that it displays the minimum viscosity of the suspension with a shear-thinning behavior, *Fazilleau et al (2006)*. This behavior means that when the shear stress imposed by the plasma flow to the drops of a liquid stream is low, the suspension viscosity is high and it decreases drastically when the shear stress increases as the drop penetrates more deeply within the plasma flow. The pH adjustment is also an important characteristic of the suspension-liquid mixing. The problem becomes complex with WC-Co particles because of the different acid/base properties of both components: *Oberste-Berghaus et al (2005)*. Indeed, WC or, more precisely, WO_3 , at its surface is a Lewis acid, while CoO is basic. Thus, a complex equilibrium between the dispersing agent and the suspension pH must be found. For example, the latter must be adjusted to less basic conditions without cobalt dissolution. Similar problems have been observed with Ni particles. When the weight % of powder increases in the suspension, its viscosity increases too.

Different products can be added to the liquid phase to modify its viscosity and/or surface tension, *Rampon et al (2008)*. For example, the addition of viscous ethylene glycol with a boiling point of 200 °C will change the suspension viscosity but at the expense of additional thermal load on the plasma, *Oberste-Berghaus et al (2006)*, while the addition of binders makes it possible to control the suspension viscosity almost independently of the dispersion.

It is also important to (i) adapt the size distribution of particles within the suspension to the potential heat transfer of the hot gases, (ii) limit the width of particle size distribution as in conventional plasma spraying in order to reduce the dispersion of particle trajectories and (iii) avoid powders that have a tendency to agglomerate or aggregate, which is often the case with nanometer sized particles, especially oxides, when prepared by chemical routes.

4.1.2 Chemical route

Another route, called Prosol process, consists in preparing a zirconia sol by neutralization of zirconium oxy-chloride in an aqueous media followed by hydrothermal crystallization, *Wittmann-Ténéze et al (2008)*. When the mixture is heated in a container at a minimum temperature of 170 °C for 20 h at a minimum pressure of 2 MPa, crystalline oxide precipitates as a mixture of monoclinic and tetragonal phases. After washing the excess of ammonium hydroxide, the particles are mixed with water with addition of hydrochloric acid (pH 3) to form a suspension.

4.1.3 Amorphous particles

Chen et al (2009) asserted that the suspension plasma spraying process, using molecularly mixed amorphous powders as feedstock, was an ideal process for the deposition of homogeneously distributed multi-component ceramic coatings.

They produced Al_2O_3 - ZrO_2 molecularly mixed amorphous powders by heat treatment of molecularly mixed chemical solution precursors below their crystallization temperatures. For that, aluminum nitrate and zirconium acetate were dissolved in de-ionized water based on molar volumes to produce a ceramic composition of Al_2O_3 -40 wt. % ZrO_2 . The resulting solution was heated at 80 °C and stirred continually to get the sol transformed into dried gel. The dried gel powders were heated at 750 °C with a heating rate of 10 °C.min⁻¹, and then held for 2 h at this temperature. The as-prepared powders were then mixed with ethanol heated to 750 °C with a loading rate of 50 wt. % and then ball-milled by using ZrO_2 balls for 24 h. XRD patterns showed that the powders were amorphous. The Al_2O_3 - ZrO_2 particles had a size distribution (d_{10} - d_{90}) of 0.71 μm with an average particle size of 0.5 μm.

4.2 Solution preparation

The precursors used in solutions include, *Ravi et al (2006)*, (i) mixture of nitrates in water/ethanol solution; (ii) mixtures of nitrates and metal-organics precursors in isopropanol (hybrid sol); (iii) mixed citrate/nitrate solution (polymeric complex) and (iv) coprecipitation followed by peptization (gel dispersion in water/ethanol).

Compared with other thermal spray techniques, solution plasma spraying using constituent chemicals mixed at the molecular level allows an excellent chemical homogeneity of coatings. It is also worth noting that aqueous solutions permit higher concentrations than organic solutions, are cheaper to produce and are easier and safer to store and handle. For example, water has been used as solvent for solutions of zirconium, yttrium and aluminum salts, *Chen et al (2007)*.

The precursor concentration in solutions can be varied up to the equilibrium saturation. A simple way to determine the equilibrium saturation concentration, is to put the solution in an evaporator at room temperature until precipitation occurs. In their study of 7YSZ solutions, *Chen et al (2008)* have considered two different precursor concentrations: a high molar concentration (2.4 M) and a low molar concentration (0.6 M). When the initial 7YSZ precursor was concentrated four times in water, the solution viscosity increases from 1.4×10^{-3} to 7.0×10^{-3} Pa. s and the surface tension decreases from 5.93×10^{-2} to 4.82×10^{-2} N.m⁻¹. Both precursors pyrolysed below 450 °C and crystallized at about 500 °C, *Chen et al(2007)*

showing that the solution precursor concentration had little effect on the precursor pyrolysis and crystallization temperatures. If a variation in precursor concentration has almost no effect on the solution specific mass and surface tension, it however brings about large variations in the solution viscosity. *Chen et al (2010)* also studied the effect of the liquid phase on the treatment of the solution in the plasma jet and got results quite similar to that already got with suspensions, i.e. droplets with high surface tension and high boiling point liquid phase experience incomplete liquid phase evaporation in the plasma jet while droplets with low surface tension and low boiling point liquid phase undergo rapid liquid phase evaporation.

5. Coating formation from suspension and solution droplets

5.1 General remarks about the in-flight treatment of nanometer or sub-micrometer particles

The coating microstructure depends on the interaction between the plasma jet and the original micrometer or sub-micrometer droplets and, then, between the plasma jet and the particles contained in the suspension or formed in the solution. These particles may have sizes in the sub-micrometer or nanometer range and form the coating when they impact on the substrate. The momentum and heat transfers between particles and plasma jet can be estimated from the drag coefficient, C_D that quantifies the resistance of particles in fluid environment and the heat transfer coefficient calculated from the Nusselt number, Nu , that is the ratio of **convective** to **conductive** heat transfer across the particle boundary. Both the drag coefficient and the heat transfer coefficient must be corrected to take into account *Boulos et al (1993)*: (i) the high temperature gradient between the gas and the particle surface. This correction is independent of the particle size and corresponds at the maximum to a 30% decrease in C_D and Nu ; (ii) the buffer effect of the vapor issued from droplet and particle. It is generally only considered for the Nusselt number and is also independent of particle size. This correction is particularly important for liquid feedstock that undergoes an intense evaporation in plasma jet; (iii) the rarefaction or Knudsen effect occurring when the ratio of the gas molecules mean free path λ to the particle diameter d_p is smaller than one. This effect is particularly important for nanometer and sub-micrometer sized particles such as particles contained in suspensions or formed in solutions.

5.1.1 Knudsen effect

The non-continuum effect can be important when the mean free path of the plasma molecules, atoms, ions, λ , is of the same order of magnitude or lower than the diameter of the particles, d_p . According to the review of *Boulos et al (1993)*, the Knudsen effect should be taken into account in the Knudsen regime characterized by $0.01 < Kn < 1.0$, where, $Kn = \lambda / d_p$. The Knudsen effect is rather low at room temperature even for particles as small as 40 nm since λ is of the order of 0.4 μm . However, under thermal plasmas conditions, λ is a few micrometers at 10 000 K (in a first approximation $\lambda \sim T/p$) and the Knudsen effect becomes important. For example, for a particle at 1000 K immersed in an Ar-H₂ plasma at 10 000 K, the correction factor for the drag coefficient is divided by a factor close to 3 when the particle diameter decreases from 1 μm to 0.1 μm and the Nusselt number by a factor 10 *Delbos et al (2006)*. The heat and momentum transfer to small particles are, thus, drastically reduced.

Moreover, these small particles that have a very low inertia, decelerate very fast and may follow the gas flow deflected by the substrate. For example in an Ar-H₂ (45–15 slm) plasma produced by a plasma torch operating at 600 A with an internal diameter of the nozzle of 6 mm, the plasma velocity decreases from 2200 m.s⁻¹ at the nozzle exit to 1500 m.s⁻¹ 15 mm downstream of the torch nozzle exit. At the same distance, the velocity of a 100-nm zirconia particle, injected close to the nozzle exit is at the most 500 m s⁻¹, and it decreases to 350 m.s⁻¹ 35 mm downstream of the nozzle exit because of the very low inertia of particle. The particles hit the substrate when certain conditions are fulfilled (see section 5.1.4).

5.1.2 Vaporization effect

The vapor surrounding the droplet or particle has a strong effect on the heat flux brought by the plasma jet as it uses part of it to heat from the particle surface temperature to the gas temperature. This effect is near independent of particle size.

5.1.3 Thermophoresis effect

The drag force is generally by far the most important force acting on particles immersed in a fluid. However, for particles below 0.1 μm, accelerated in a plasma jet, the thermophoresis force can become important *Boulos et al (1993)* in areas where steep temperature gradients exist, such at the limit between the plasma core and its plume. The plasma core corresponds roughly to the jet zone where temperatures are over 8000 K corresponding, for most plasma gases except pure Helium, to an electrical conductivity over 1 kA.V⁻¹.m⁻¹. The thermophoresis force tends to eject small particles into the plasma plume where gas temperatures and velocities are lower, as shown in Figure 8.

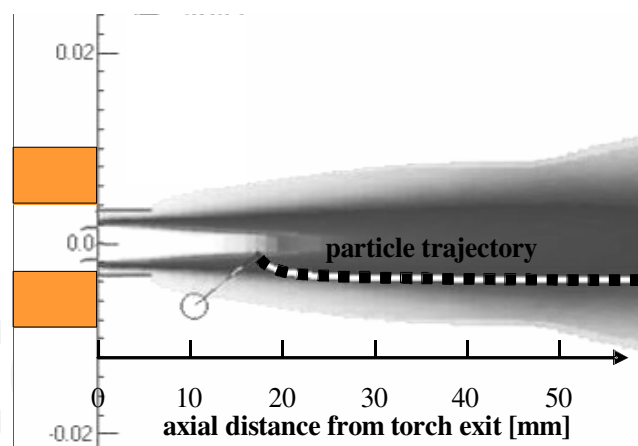


Fig. 8. Schematic of the Thermophoresis effect

5.1.4 Stokes effect

Because of their low inertia, small particles can follow the gas flow that travels parallel to the substrate surface without impacting it. To hit the substrate, particles must cross the boundary layer that develops at the substrate surface. The Stokes number characterizes the

behavior of particles **suspended** in a fluid flow. It is defined as follows:
$$St = \frac{\rho_p \cdot d_p^2 \cdot v_p}{\mu_g \cdot l_{BL}}$$

where indexes p and g are related to particles and gas, respectively, ρ is the specific mass ($\text{kg}\cdot\text{m}^{-3}$), d the diameter (m), v the velocity ($\text{m}\cdot\text{s}^{-1}$), μ the molecular viscosity ($\text{Pa}\cdot\text{s}$) and l_{BL} the thickness of the flow boundary layer in front of the substrate (m). When St is higher than 1, that is when particle velocity is high enough, particles can detach from the flow and hit the substrate.

For the Ar-H₂ plasma already considered the Stokes number of particles 0.3 μm in diameter is equal to 1 when their velocity reaches $300\text{ m}\cdot\text{s}^{-1}$ assuming a flow boundary layer at the substrate surface in the order of 0.1 mm, *Delbos et al, (2006)*. It is thus of primary importance that the particles have high velocities just prior to impact, especially when their size decreases to sub-micrometer or nanometer values. As the inertia of small particle is very low and the boundary layer thickness in front of the substrate decreases, in a first approximation, as the inverse of the square root of the gas velocity, the substrate must be located at short distances of the torch nozzle exit. For example, with stick-type cathode plasma torch, *Fauchais et al (2008)*, spray distances between 30 and 50 mm are commonly used. Accordingly, heat fluxes imposed by the plasma flow on the forming coating and on the substrate are very high, as illustrated in Figure 9. Compared with micrometer-sized conventional coatings sprayed on substrates located at 100–120 mm and subjected to heat flux below $2\text{ MW}\cdot\text{m}^{-2}$, the very high heat fluxes (up to $40\text{ MW}\cdot\text{m}^{-2}$) imposed on suspension plasma-sprayed coatings contribute to their morphology modification.

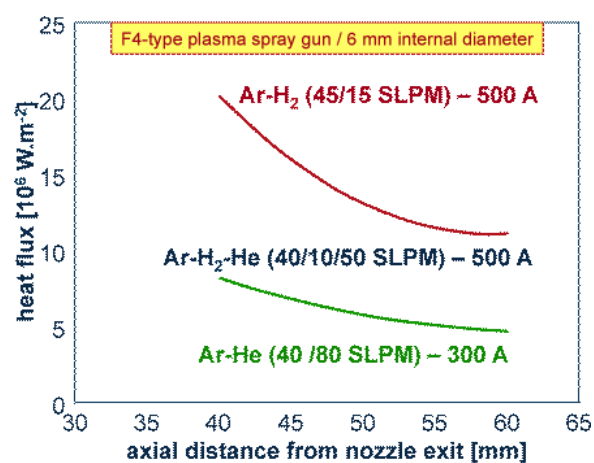


Fig. 9. Variation with the spray distance of the heat flux imparted to a surface by a stick-type cathode plasma torch (6 mm i.d. anode–nozzle) working with Ar-H₂, Ar-He and Ar-He-H₂ plasma-forming gas mixtures *Fauchais et al (2008)*.

5.2 Radio frequency plasma spraying

5.2.1 Suspensions

Bouyer et al (1995 and 1997) were the first to propose the production of hydroxyapatite (HA: $\text{Ca}_{10}(\text{PO}_4)_6(\text{OH})$) coatings using the technique called suspension plasma spraying (SPS). The process involved the injection of the HA material in the form of an atomized colloidal water suspension into the center of an inductively coupled r.f. plasma discharge. This process is a powderless (colloidal suspension) plasma-spraying technique. The HA suspension was brought into the plasma discharge core via a gas-atomizing probe fed with a peristaltic pump. As mentioned previously the relative gas-drops velocity was too small ($<50\text{ m}\cdot\text{s}^{-1}$) to

fragment the drops ($< 100 \mu\text{m}$). The latter were successively flash-dried, melted, deposited on the substrate to be coated or collected in-flight as spherical particles. The process took full advantage of the inherent features of the induction plasma, which allows sufficient time for the droplet drying and melting steps. The first parts of the drop trajectories took place in a pure Ar plasma with a rather low heat transfer and it was only downwards that heat transfer increased thanks to the diffusion of the diatomic sheath gas in the torch central part. Figure 10a shows the three main routes for HA deposit preparation, while Figure 10b presents the suspension with needles of HA. The SPS route is, by far, the simplest and least costly, and it also eliminates many potentially contaminating steps in coating preparation. Authors showed the feasibility of suspension plasma spraying for HA coatings with high deposition rates ($> 150 \mu\text{m}\cdot\text{min}^{-1}$) and also for spheroidized powder production. The use of a r.f. plasma torch made it possible to use oxygen as sheath gas. The decomposition of HA during plasma treatment could be either avoided or at least minimized by using appropriate plasma gases, i.e. a plasma-sheath gas mixture with moderate enthalpy and high oxidizing potential. For example hydrogen acts as harmful gas for HA stabilization, while oxygen is beneficial. In addition, the presence of water in the suspension contributed to the resistance of the apatite structure to decomposition during the high-temperature treatment by maintaining a high partial pressure of water vapor in the deposition reactor.

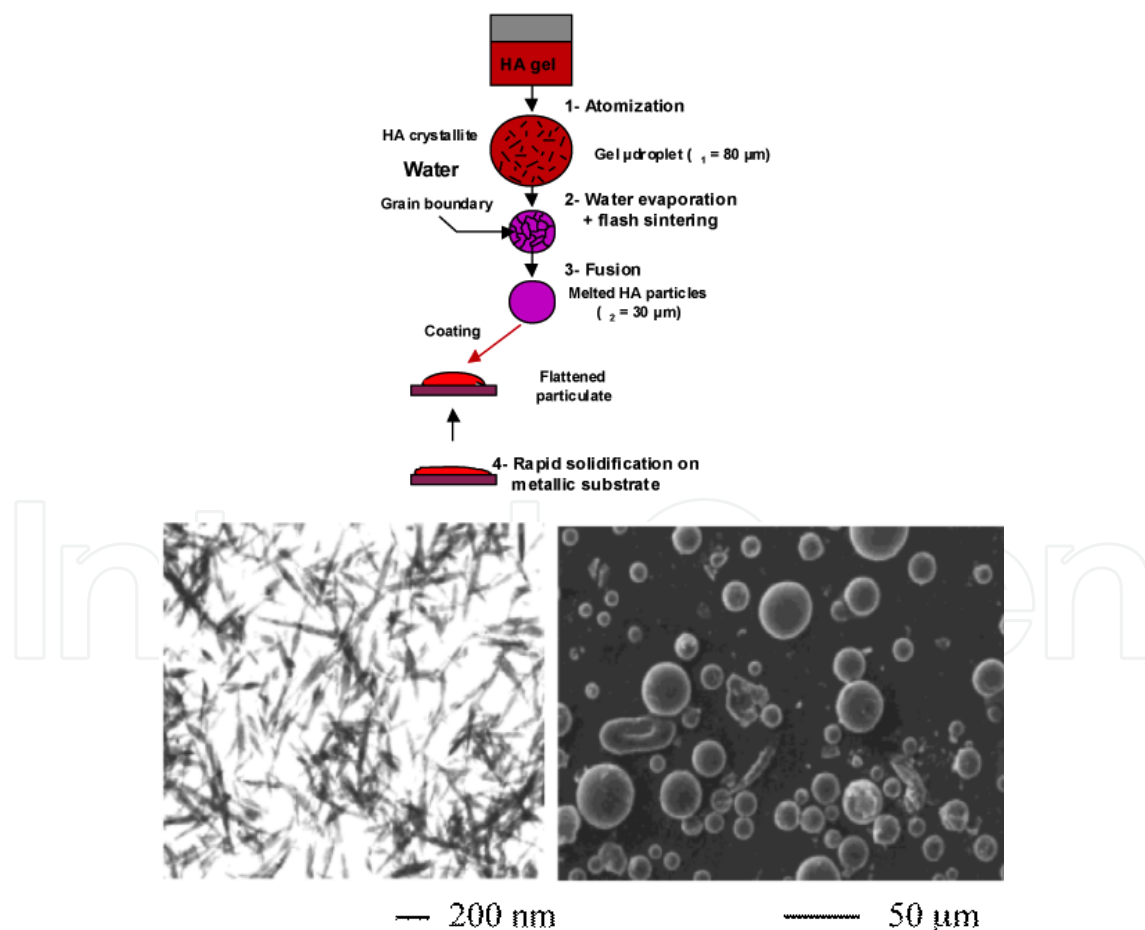


Fig. 10. (a) Schematic routes for HA coating deposition by suspension plasma spraying with r.f. plasma torch, (b) Suspension of HA needle shaped, (c) Spheroidized particles collected in the reactor, *Boyer et al (1995, 1997)*.

Schiller et al (1999), using a reactive precursor suspension of MnO_2 powder in an ethanol solution of LaCl_3 prepared perovskite powders and coatings. The powder completely melted in the plasma and the LaMnO_3 perovskite phase was formed as primary phase. A certain amount of additional phases (La_2O_3 , ...) were also present in the coating. The purity of the perovskite coatings could be further enhanced through a post-treatment using plasma with a high content of oxygen (80%). However further works are still necessary to completely prevent the formation of La_2O_3 , control the coating porosity and dope LaMnO_3 with strontium.

This spray technique has also been used by *Bouchard et al (2006)* to produce perovskite cathode materials ($\text{La}_{0.8}\text{Sr}_{0.2}\text{MnO}_{3-\delta}$, $\text{La}_{0.8}\text{Sr}_{0.2}\text{FeO}_{3-\delta}$, and $\text{La}_{0.8}\text{Sr}_{0.2}\text{CoO}_{3-\delta}$), with accurate control of deposit stoichiometry. Most particles of the plasma-synthesized powders were about 63 nm in size, with an average grain size of 20 nm. The plasma-synthesized powders were almost globular in shape, and their BET specific surface areas were $\sim 26 \text{ m}^2\cdot\text{g}^{-1}$, i.e., about twice that of powders prepared by other routes. *Jia and Gitzhofer (2010)* elaborated coatings by r.f. plasma spraying of suspensions made of gadolinia-doped ceria (GDC) particles with a mean size of $0.6 \mu\text{m}$ dispersed in distilled water. The resulting coating (Figure. 11a) consisted of layered splats with diameters ranging from 0.2 to $2 \mu\text{m}$ corresponding to a flattening ratio below 2.7.

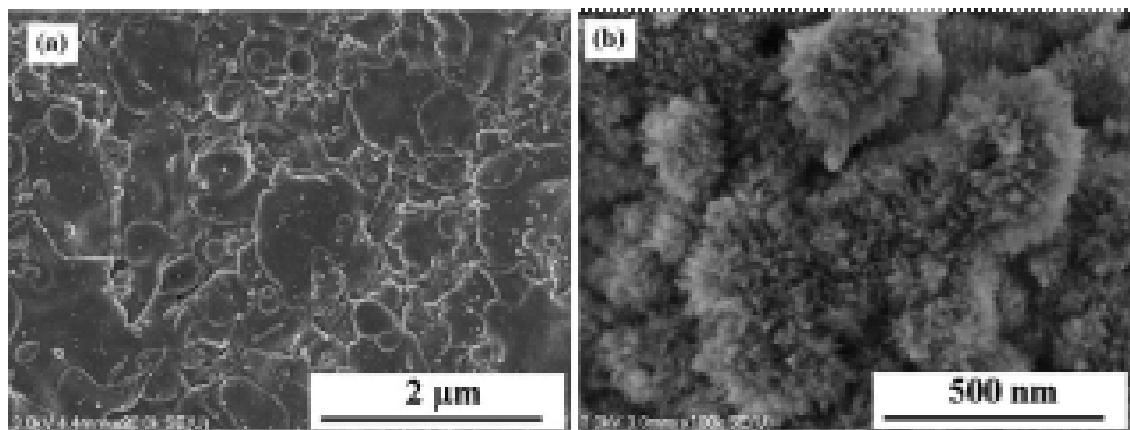


Fig. 11. Field emission scanning electron microscope (FESEM) micrograph of r.f. **suspension** plasma-sprayed gadolinia-doped ceria coating top surface, (b) FESEM micrographs of r.f. **solution** plasma sprayed GDC coating top surface *Jia and Gitzhofer (2010)*.

5.2.2 Solutions

In Solution r.f. Plasma Spraying, called SolPS process by *Jia and Gitzhofer (2010)*, GDC solutions of nitrate hexahydrate were completely vaporized in the plasma. Nano-structured GDC particles were synthesized in flight by homogeneous nucleation from the supersaturated precursor vapor and build up a coating with high porosity (Figure 11b) when impacting on a substrate. The formation of globular GDC coatings was observed over the entire experimental range of this study. Similarly *Shen et al (2011)* have r.f. plasma sprayed solutions of Lanthanum strontium cobalt iron oxide (LSCF: $\text{La}_x\text{Sr}_{1-x}\text{Co}_y\text{Fe}_{1-y}\text{O}_{3-\delta}$) and GDC. A homogeneously mixed nanometer sized composite GDC/LSCF powder was obtained without a prolonged period of mechanical mixing. The nanometer-sized powders exhibited a perovskite structure, a fluorite structure and separated GDC and LSCF phases.

When using a low solution-feeding rate, nanometer-sized powders with different compositions were easily synthesized by only adjusting the metal nitrate concentrations in the precursor solution. All synthesized powders had spherical particles with diameter between 10 and 60 nm regardless of their composition. The deposited coating had a homogeneous nano-cauliflower structure, similar to that presented in Figure 11b, with an average porosity of 51%.

5.3 Direct current (dc) plasma spraying

In dc plasma spraying, as explained in section 3.2.4, the fragmentation of the liquid feedstock injected in the transverse plasma jet is a few orders of magnitude faster than vaporization and stops, depending on plasma velocities when particles reach diameters ten micrometers or so, corresponding to $We < 12$.

5.3.1 Suspensions

a. Solid particles in-flight

Once the liquid feedstock in the form of drops or liquid jet penetrates the hot gas flow, if $We > 12$, it is fragmented into droplets with a size that decreases as they go deeper in the plasma jet. The liquid injection location, either close to the anode-nozzle exit or farther downstream, plays an important role in the fragmentation process as the later depends on the momentum density ($\rho_g \cdot v_g^2$) of the plasma jet at the liquid location and the velocity of the gas, v_g , decreases rather fast with the distance from anode-nozzle exit, because of the jet expansion. The droplets issued from liquid fragmentation have trajectories that are widely dispersed within the plasma jet. Once the liquid phase is completely vaporized, the solid particles contained in each droplet follow different trajectories in the plasma jet fringes or hot core of the jet and can be ejected from the hot core because they travel in area of high temperature gradients as shown in Figure 8. Along these trajectories solid particles are heated and accelerated by the hot gas flow; their initial velocity is that of their 'mother' droplet prior to its total vaporization. When agglomerates are formed, they tend to explode upon complete vaporization of the liquid phase in particular if the nanometer-sized particles of the suspension have been prepared by soft-chemical routes *Delbos et al (2006)* and this phenomenon increases the dispersion of the solid particles constituting the agglomerates. When the sprayed material is collected during a short period (e.g. a few tenths of a second) on a fixed substrate, only splats are observed in the central part of the collecting area while around it only spherical and un-melted particles are observed *Fauchais et al (2008)*. The spherical particles correspond to particles that melt in the plasma jet but are re-solidified before their impact on the substrate while the un-melted particles mainly result from drops fragmented in the jet fringes where the solid particles contained in the drops are insufficiently treated but, often heated enough to stick to the substrate or the coating under formation. Obviously, some additional studies are necessary to further document the organization of the particles upon complete liquid phase vaporization.

When the suspension is injected axially in the plasma jet as with the Mettech plasma torch (see section 2.2) the droplets are also highly dispersed in the whole plasma jet including in the cold boundary layer of the flow because of the flow turbulences, and the thermophoresis effect also takes place. A numerical study of Xiong and Lin (2009) suggested that the optimal

diameter of Al_2O_3 particles for axial injection-suspension plasma spraying is about $1.5 \mu\text{m}$ for 'optimum' coating characteristics. Under these conditions, at the appropriate spray distance, particles can impact at high velocity in a fully molten condition. The small particles ($< 500 \text{ nm}$) do not flatten so effectively, because they attain lower momentum and because they may re-solidify before impact, on account of their low inertia. Large particles and agglomerates ($>2.5 \mu\text{m}$), by contrast, remain partly or entirely un-melted.

b. Bead formation

A line-scan-spray experiment makes it possible to evaluate the degree of melting of particles; it can consider either a simple bead resulting from one pass of the torch in front of the substrate or overlapped beads resulting from successive passes of the torch. The bead thickness depends on the torch operating conditions and on the relative torch to substrate velocity, the number of passes, the suspension flow rate and the injection parameters, the mass loading of powder particles in suspension, the size distribution of particles. The bead profile generally fits rather well with a Gaussian profile.

To study the spray bead manufacturing mechanisms, *Tingaud et al (2008)* made a suspension of alumina of angular single mono-crystalline $\alpha\text{-Al}_2\text{O}_3$ (P152 SB, Alcan, Saint-Jean de Maurienne, France) of $d_{50} = 0.5 \mu\text{m}$ dispersed in pure ethanol with an electro-steric dispersant. The powder mass fraction in suspension was 10 wt%. The suspension was sprayed on a 304L stainless steel substrate preheated with the plasma jet at $300 \text{ }^\circ\text{C}$ before spraying, to eliminate adsorbates and condensates *Chandra and Fauchais (2009)*. As expected, spray parameters and substrate parameters conditioned the spray bead morphology.

In the spray beads shown in Figure 12, two regions could be identified, that corresponded to adherent deposit and powdery deposit. Powdery deposits located at the edges of the spray bead corresponded to precursors traveling in the low-temperature regions of the plasma flow. The central part of the bead was relatively dense and made of splats with a few spherical particles re-solidified in flight and angular un-melted particles that have travelled in colder zones. The splats corresponded to particles adequately (i.e. well-melted) treated in the plasma core. At mid-height of the spray bead, the coating was less dense with many un-melted particles and at its edges it was fully powdery.

To get coatings with good cohesion, the central part of spray beads must contain as much as possible fully or near molten particles at impact.

In the example shown in Figure 12, the densest coating was obtained at a spray distance of 30 mm where the plasma heat flux to substrate reaches 30 MW.m^{-2} . The coating density seems to slightly decrease when the mass load of suspension increased from 5 wt. % to 10 wt. %, very likely because of a loading effect. The spray beads on substrate located at 40 mm are thicker but less dense due to the incorporation of more untreated particles.

The particle melting was also deeply affected by the characteristics of the powder used in the suspension, particularly its primary particle size distribution and its agglomeration behavior that can be characterized by the size and strength of agglomerate. With the short spray distances used in suspension plasma spraying, the coating surface temperature reaches $700\text{--}800 \text{ }^\circ\text{C}$, as measured with infrared pyrometer during two successive passes of the plasma torch on the substrate. It is worth noting that droplets reaching the substrate

without being completely vaporized before impact will be vaporized on the surface of the hot coating under formation. Thus, if the solid particles contained in these droplets do not rebound on the surface, they will be incorporated into the coating and create defects. Such temperatures, as shown in section 5.3.1.2 also affect the splat formation and thus coating formation.

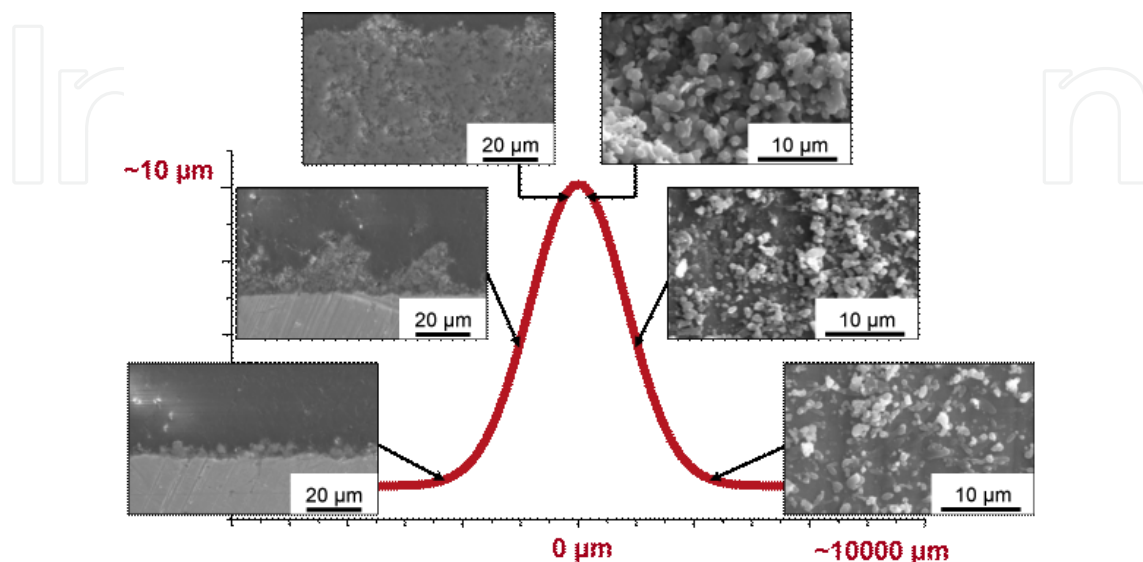


Fig. 12. Al_2O_3 suspension plasma-sprayed coating microstructures for two particle mass loads (5 and 10 wt%) and three spray distances (30, 40, 50 mm). Spray conditions are depicted in Figure 32 caption *Tingaud et al (2008)*.

It was also observed that the use of water instead of ethanol as liquid phase in suspension plasma spraying brings about more porous coatings than those achieved with ethanol-based suspensions if the electric power level input to the plasma gas was not increased *Tingaud et al (2008)*.

c. Coatings formation

When spray beads overlap during spraying, the poorly treated particles i.e. mainly unmelted, partially molten and re-solidified particles, generally located at the bead edges, are embedded in the coating during deposition. The different passes may thus be separated by porous and poorly cohesive layers that may induce voids and delamination in the upper layer as shown in Figure 13(a). The probable explanation is depicted in Figure 14a, showing how, according to the spray pattern, the poorly treated particles travelling in the jet fringes are deposited at the surface of the hot previous pass and may stick on when its temperature is higher than 800–900 °C. The following well-molten particles, which have travelled in the warm zone of the plasma jet, form the next pass on the powdery layer deposited by the preceding particles travelling in the jet fringes. It is worth noting that the first pass is deposited on the substrate temperature that is generally still below 300 °C and almost no sticking of poorly treated particles occurs. So, the interface between the substrate and the first pass is relatively clean compared with that between next passes. When the spray pattern is adapted, in particular to reduce the mean surface temperature of the coating under construction, it is nevertheless possible to get rid of most of the powdery layer between passes and obtain rather thick and dense coatings, as illustrated in Figure 13b.

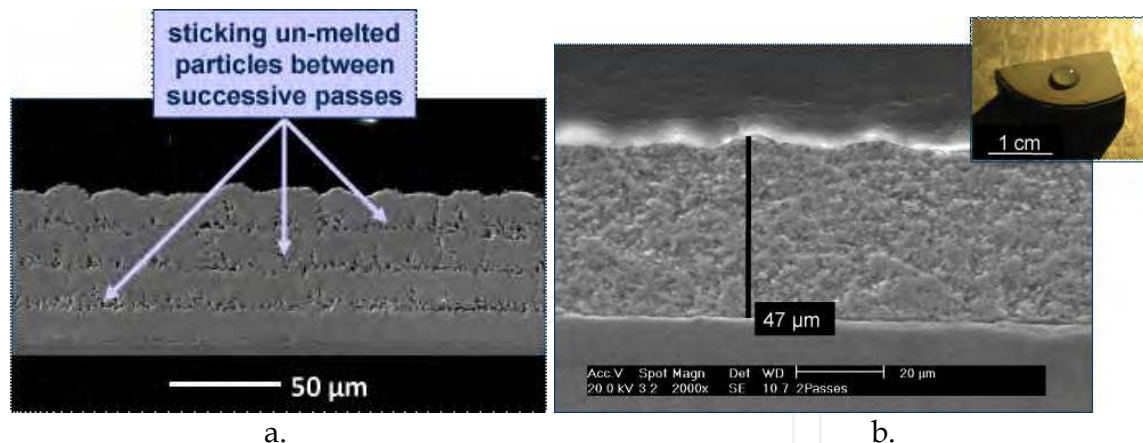


Fig. 13. Yttria Partially Stabilized Zirconia (YPSZ) coatings (4–5 passes) obtained with the same Et-OH suspension Unitec 0.02 (Unitec Ceram, Stafford, UK, fused and crushed, $d_{50} = 0.39 \mu\text{m}$) sprayed under different operating conditions with Plasma-Technik F4-type torch (nozzle i.d. 6 mm). (a) Ar-He (30–30 slm, 700A, $v_{inj} = 33.5 \text{ m.s}^{-1}$), (b) Dense and thick Y-PSZ (8 wt%) coating deposited under the spray conditions depicted in Figure 13a, the spray pattern being adapted to avoid powdery layers deposited between successive passes Fauchais *et al* (2008).

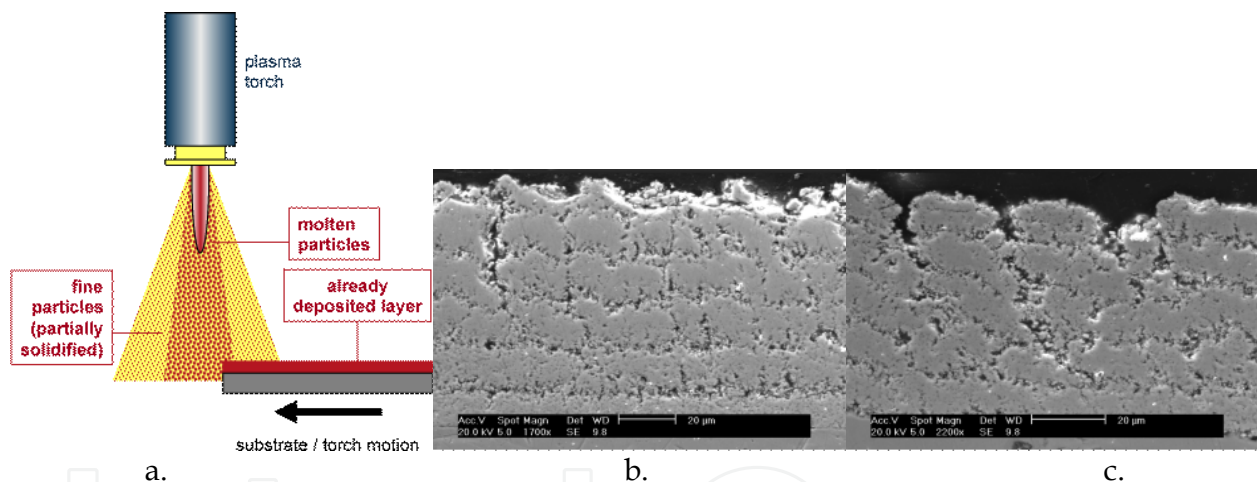


Fig. 14. (a) Schematic explanation of the deposition on each pass of a powdery layer due to the sticking of poorly treated particles in the jet fringes preceding the deposition of the well-molten particles, (b) YSZ coatings (4–5 passes) obtained with the same suspension as that of Figure 13 Ar-H₂ (45–15 slm, 500A, $v_{inj} = 33.5 \text{ m.s}^{-1}$), (c) Ar-H₂ (45–15 slm, 500A, $v_{inj} = 26.6 \text{ m.s}^{-1}$) Fauchais *et al* (2008).

When the suspension is sprayed with highly fluctuating plasma jet as Ar-H₂ plasma ($\Delta V/V_m \sim 1$ with an Ar-H₂ plasma against 0.25 with an Ar-He plasma), more powdery material is deposited between successive passes and the pore level is higher as shown in Figure 14(b). The situation becomes worse in terms of poorly-treated particle deposition when the suspension is injected in Ar-H₂ plasma with a lower injection velocity that limits the suspension penetration in the plasma jet, as shown in Figure 14c. The situation is even worse when using a suspension containing particles that agglomerate easily with a rather broad distribution of agglomerate sizes between 0.01 and 5 μm . The structure of each pass

consists, then, of some sort of columnar structures or ridges, with columns 10–20 μm in diameter made of layered splats and particles *Delbos et al (2006)*.

The high transient heat flux (see Figure 9) imposed by the plasma jet to the substrate and coating in formation affects the coating construction. Indeed, such heat flux leads to coating surface transient temperatures over 1500 $^{\circ}\text{C}$ *Etchart-Salas (2007)*. When Y-PSZ splats are collected on a substrate attached at the extremity of a pendulum crossing the jet at 1 $\text{m}\cdot\text{s}^{-1}$, the flattening degree is below 2 and is mostly less than 1.5 while it is generally about 4–5 for ceramic particles with size ranging between 10 to 50 μm . This low value is explained by the low inertia and the high surface tension of very small particles. Another important feature to be underlined is that splats with diameter smaller than 2 μm no longer exhibit cracks that would normally be present due to splat quenching stress. According to splat formation mechanisms, it could be expected that suspension plasma-sprayed coatings present a lamellar structure similar to that of conventional coatings made with micrometer-sized particles. In fact the structure of coatings is different, for example, in suspension plasma spraying of Y-PSZ particles, the first deposited layers that have a thickness of about 400 nm, exhibit a columnar structure, as expected from splats layering, while the following layers exhibit a granular structure (Figure 15). This may be explained by a recoil phenomenon experienced by the impinging particle, after flattening and prior to solidification, due to a surface tension effect, which is emphasized for sub-micrometer-sized particles, while, due to the important transient heat flux, the flattening particle cooling is delayed. Similar results were observed with alumina suspensions, where granular particles and splats were observed in coating structures *Darut et al (2009)*. The coating was a mixture of α and γ phases (about 50% of each), in spite of the fact that most particles at impact formed splats. In conventional coatings, mostly made of γ -alumina phase, the transformation of this phase into α occurs when the coating is reheated over 1000 $^{\circ}\text{C}$ (however, the transformation takes a few seconds).

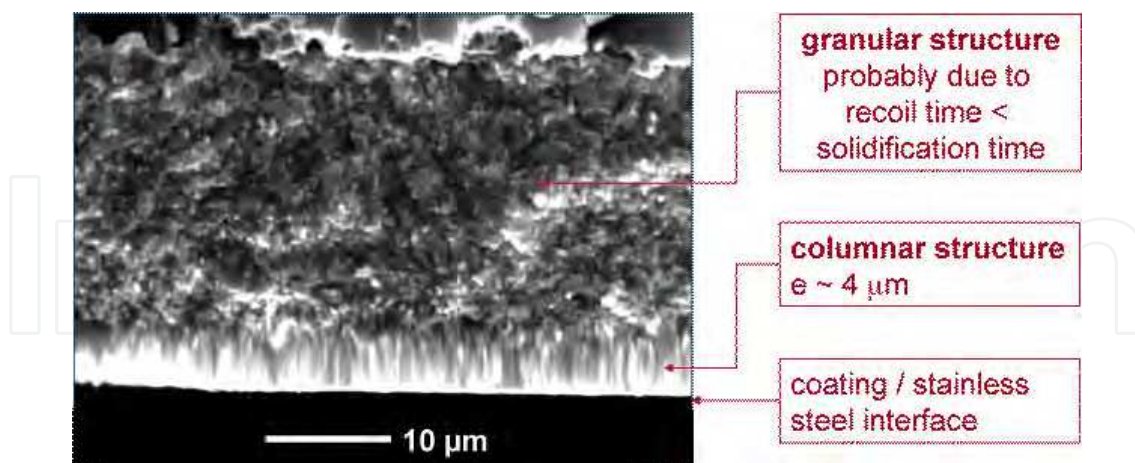


Fig. 15. Fractured cross-section of Y-PSZ suspension coating plasma-sprayed on stainless steel 316L substrate disposed 40 mm downstream of the nozzle exit. The suspension consisted of sub-micrometer-sized attrition milled particles (0.2–3 μm) in ethanol and was sprayed with an Ar–H₂–He plasma *Delbos et al (2006)*.

As in conventional thermal spraying the substrate roughness must be adapted to the sizes of the solid particles of the suspension. Works developed at SPCTS Laboratory of University of

Limoges. *Brousse et al (2008)* showed, that coating architecture was very sensitive to substrate roughness. Large columnar stacking defects developed from the valleys of the surface due to a 'shadow' effect propagating through the coating when the substrate surface roughness was higher than the average diameter of the feedstock particle, as depicted in Figure 16a. Reducing the stacking defects to enhance gas tightness (hermeticity) required spraying onto smooth polished substrates. For example, when decreasing the ratio of the roughness average R_a of the substrate to the feedstock particle average diameter d_{50} from 75 to 2 for Y-PSZ suspension coating, the leakage rate decreased from 0.5 to 0.02 Mpa.L.s⁻¹.m⁻¹. However, if no stacking defects can be observed on the SEM picture of Y-PSZ suspension coating corresponding to $R_a/d_{50} = 2$ (Figure 16c), it does not mean that they do not exist, as confirmed by a non-negligible leakage rate. Thus a compromise has to be found between d_{50} and R_a to get rid of these stacking defects.

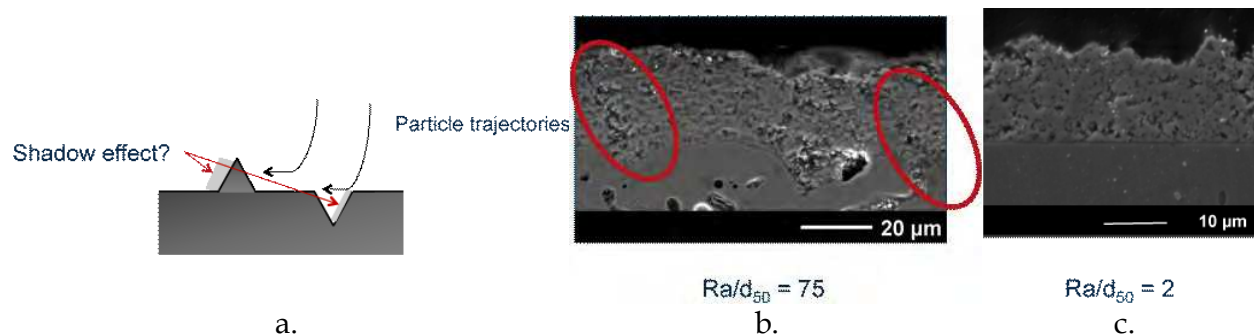


Fig. 16. (a) Principle of shadow effect, (b) Y-PSZ coating sprayed onto a substrate exhibiting an average substrate roughness 40 times higher than the feedstock particle average diameter (R_a/d_{50}): columnar stacking defects develop through the coating thickness, (c) No shadow effect when $R_a/d_{50} = 2$, by *Brousse et al (2008)*.

5.3.2 Solutions

a. Drops and droplets in flight

Ozturk and Cetegen (2004, 2006) have modeled the behavior of single precursor droplets injected into high-temperature gas jets. The processes undergone by the drops axially or radially injected into the gas flow can be divided into three distinct phases: (i) The first phase is the aerodynamic break-up, which, as for suspension droplets, depends on the Weber and Ohnesorge numbers (see section 3.2.4). (ii) The second phase is droplet heating and surface evaporation in the hot gas jet stream. Loss of liquid phase from the surface concentrates the salt solutes, progressively leading to precipitation of the solute as it reaches a super-saturation level. Precipitation may occur in all regions of the drops or droplets that exceed the equilibrium saturation concentration, according to the homogeneous precipitation assumption, *Saha et al (2009)*. Depending upon the droplet size and the mass transport characteristics within the droplet, different precipitate morphologies can be obtained: shell type morphologies or spherical precipitates. The thickness of the shell can be predicted from the homogeneous nucleation hypothesis unlike the void content. (iii) The third phase is the further heating of the precipitates in the hot gases before their impact on the substrate surface.

Particle morphologies depend on the different processes undergone by the droplets in the hot gas that are linked to their trajectories. According to *Saha et al (2009)*, they include solid particles, hollow shells and fragmented shells as shown in Figures 17(a) to (c). Small droplets with high solute diffusivity exhibit a propensity to precipitate volumetrically and form solid particles as shown in Figure 17(a). Rapid vaporization combined with low solute diffusivity and large droplet sizes can lead to a significant increase in solute concentration near the droplet surface resulting in surface precipitation and formation of a crust around the liquid core of the droplet. The crust/shell may have varied levels of porosity. Shells having low porosity usually rupture due to internal pressurization to form shell fragments (path I in Figure 17b). Shells that are completely impervious rupture and secondary atomization of the trapped liquid core may be observed (path III in Figure 17b). For shells with a high level of porosity, internal pressure rise is counterbalanced by the vapor venting through the pores and resulting in hollow shells (path II in Figure 17b). For particular precursors, elastic inflation and subsequent collapse and rupture of the shell can also be observed (Figure 17c). The particle morphology resulting from droplet processing is hence sensitive to the solute chemistry, mass diffusivity, solute solubility, droplet size, thermal history, injection type and velocity *Saha et al (2009)*. In summary, according to *Saha et al (2009)* the final coating microstructure depends on the size of the droplets, not on whether they follow a trajectory centered on the torch centerline axis or a deviated one after primary precipitation. Globally, droplets in the size range 5 or 10 μm get completely pyrolysed before reaching the substrate, while the 20 μm and larger droplets remain partially pyrolysed. However the initial solution concentration plays a key role in droplet pyrolysis. A high or close to the equilibrium saturation concentration tends to produce volume precipitation *Chen et al (2008)*. Microstructures of the collected solution plasma-sprayed coatings of YSZ on substrates at room temperature from low and high concentration solutions, respectively, are presented in Figures 4 and 5 of the paper of *Chen et al (2008)*. No splats are observed out of the central zone of the deposited bead with the low concentration solution precursor, mainly composed of ruptured bubbles and a small volume fraction of solid spheres ($< 0.5 \mu\text{m}$). The deposited bead central zone made from the high-concentration solution is mainly composed of overlapped splats, with an average diameter ranging from 0.5 to 2 μm , and a small amount of un-melted solid spheres ($< 0.5 \mu\text{m}$). The deposited bead edges from both dilute and concentrated solutions are made of un-pyrolysed precursors containing significant amounts of water. The mud-like cracks presented at the edges are the result of shrinkage due to liquid phase evaporation on the substrate.

b. Coating formation

Xie et al (2004) studied a single deposited bead from YSZ solutions resulting from one pass of the torch in front of a polished substrate and overlapped beads resulting from successive passes. The resulting spray beads can be divided into adherent deposits (bead central part) and powdery deposits (bead edges) that correspond to the hot and cold regions of the plasma jet, respectively. *Chen et al (2008)* identified four deposition mechanisms: (i) smaller droplets that undergo further heating to a fully molten state and crystallize upon impact to form ultra-fine (0.5–2 μm average diameter) splats; (ii) at certain spray distances, droplets undergo re-solidification and crystallization before impact upon the substrate to form fine crystallized spheres; (iii) droplets entrained in the cold regions of the thermal jet where they experience sufficient heating to cause solute evaporation leading to the formation of a gel

phase, deposited on the substrate. Some droplets also form a pyrolysed shell containing un-pyrolysed solution that fractures during deposition; (iv) some precursor solution droplets can reach the substrate in liquid form, having undergone none of the aforementioned processes.

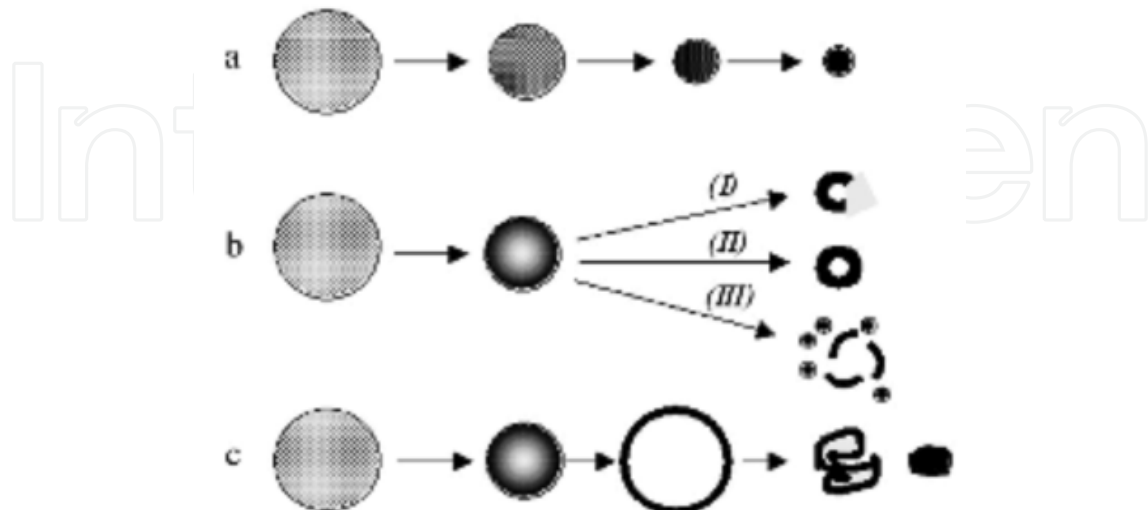


Fig. 17. Different routes for a droplet for vaporization and solid precipitation: (a) uniform concentration leading to solid particles by volume precipitation. (b) Super-saturation near the surface: (I) low permeable shell leading to fragmented shell formation, (II) high permeable shell leading to un-fragmented shell formation, (III) impermeable shell leading to droplet internal heating, pressurization and droplet breakup, secondary atomization. (c) Elastic shell formation causing inflation and deflation by solid consolidation *Saha et al (2009)*.

Most works dealing with solution plasma spraying use atomization to inject solutions into conventional dc plasma jets and, as underlined in section 3.2.1, very different size, velocity and trajectory distributions can be obtained, the best coatings being obtained with narrower droplets, *Jordan et al (2007)*. A high concentration precursor (close to equilibrium saturation) is also important to promote volume precipitation leading to fully melt splat microstructure and high density coating, *Chen et al (2008)*. The type of liquid phase also plays a key role: droplets with a high surface tension and high boiling point liquid phase experience an incomplete liquid phase evaporation process in the thermal jet and forms a mud-like cracked film upon impacting the substrate leading to a porous coating. Droplets created from a low surface tension and low boiling point liquid phase undergo rapid liquid phase evaporation, solute precipitation, pyrolysis, melting process in the plasma jet and form splats upon impact on the substrate, the stacking of which results in a dense coating. At last the substrate and coating temperature during spraying is also very important. Non-pyrolysed materials are pyrolysed at the substrate surface and form aggregates when the substrate temperature is above the precursor pyrolysis temperature. Pyrolysis also occurs when reheating the coating by successive torch passes *Chen et al (2010)*. Under the repeated processing by the high-temperature thermal jet, the mud-like film for example formed when spraying droplets with a high surface tension and high boiling point liquid phase, evaporates, pyrolyses and crystallizes on the substrate and brings about porous coatings. To conclude, the amount of non-decomposed precursor can be controlled by the spray

parameters, primarily liquid/gas stream injection momentum densities, spray droplet size dispersion and precursor concentration.

6. Characterization of nanostructures

The knowledge of structural characteristics and functional properties of nanometer-sized coatings is fundamental whatever the envisaged applications and manufacturing processes. The thermo-mechanical behavior of coatings and, in the case of thermal barrier coatings, their thermal insulation performance are mostly related to the void architecture or void networks (for example, see *Rice (1996)*).

The main question is the following: are methods used for conventional micro-structured thermal sprayed coatings suitable for nanostructured coatings? For more details about possible answers the reader is referred to the paper of *Fauchais et al (2010)*. The various possibilities are briefly presented below:

- The observation of coating cross-section mostly by using scanning electron microscopy, SEM, coupled with appropriate image treatment and statistical models makes it possible to quantify the void content as a function of the void size and, with some specific models, of their shape and crack density and orientation. However, the image characteristic dimension should be between 10 and 15 times larger than the objects of the voids to be analyzed in order to have a representative elementary volume (REV) of the structure. Actually the resolution is limited to features larger than $0.1\mu\text{m}$, average value, which is by far not sufficient to characterize nanometer-sized coatings. Also cutting and polishing of nanostructured coatings are more difficult because their toughness can be 4 to 8 times larger than that of conventional ones.
- Archimedean porosimetry and electrochemical impedance spectroscopy are based on the penetration of a liquid within the coating. However, the simplistic test of de-ionized water droplet percolation (see the top of Figure 13b) through the deposit permits the determination of the smallest open pore diameter into which the water is able to percolate. For example at atmospheric pressure (about 10^5 Pa), pure water percolates into open voids of equivalent diameter equal to or larger than $1.5\mu\text{m}$, which is by far larger than most of the open voids in nanostructured coatings.
- Mercury intrusion porosimetry (MIP) presents the advantage of covering a large void size range, theoretically from a few nanometers to a few tens of micrometers and has been largely used to quantify void network size distribution of nanostructured coatings (see, for example, *Portinha et al (2005)*).
- Gas pycnometry, generally using helium, is based on gas pressure measurement in an unvarying gas volume measured by implementing a cell, which either does or does not contain the sample. This technique allows the quantification of the open void content of coatings and does not present any relevant drawback. It has been successfully implemented on nanometer-sized suspension plasma-sprayed coatings *Bacciochini et al (2010)*.
- Small angle neutron scattering (SANS) is an advanced technique to assess the void characteristics of thermal spray coatings including surface area distribution and orientation distribution. This technique has been successfully implemented in plasma-sprayed micrometer-sized YSZ thermal barrier coatings. Due to its capabilities

Hammouda (2008), this nondestructive technique is able to probe the nano-void size distribution in coatings. To the best of the authors' knowledge, nevertheless, this technique has not been implemented yet.

- Ultra-Small Angle X-ray Scattering (USAXS) is a nondestructive characterization technique recording elastic scattering of X-rays induced by compositional and structural in-homogeneities *Ilavsky J. et al (2009)*. USAXS has been successfully implemented in quantifying void size distribution in YSZ (d_{50} : 50 nm) suspension plasma-sprayed coatings (see, for example, *Bacciochini et al (2010)*) and showed that about 80% of voids, in number, exhibited characteristic dimensions smaller than 30nm, the largest voids in the coatings having characteristic dimensions of a few hundred nanometers. The total void content was between 12.9% and 20.6%, with median diameters ranging from 270 to 400 nm and most of the voids (in number) had characteristic dimension smaller than 20 nm, contrary to micrometer-sized plasma sprayed coatings, which do not contain significant contribution of nano-voids smaller than 20 nm. Such results are difficult, if not impossible, to obtain from other characterization techniques, since they do not have the capability of USAXS to address with a very high resolution the whole set of scatter features (voids in this case) regardless of their characteristics (open, connected or closed).

7. Potential applications

As for all new processes, the mean time for application is between 20 and 25 years, thus it is quite understandable that the solution and suspension plasma spraying processes that are still under development have essentially potential applications. They are mainly in the following fields: wear-resistant, thermal barrier, corrosion-resistant, bioactive, photocatalytic, and electrochemically functional coatings *Gell et al (2008)*, *Vaßen et al (2010)*, *Fauchais et al (2011)*, *Killinger et al (2011)*. A few examples are presented here to illustrate these various fields.

7.1 Thermal barrier coatings (TBC)

Yttria-stabilized or partially stabilized zirconia (YSZ or YPSZ) coatings deposited by solution and/or suspension spraying has been intensively studied. *Ben-Ettouil et al (2009)* investigated the thermal shock resistance of Y-PSZ suspension plasma-sprayed coatings (feedstock particles $d_{50} = 50\text{nm}$) and found that their resistance to isothermal and thermal shocks was higher for coatings with lower crack density. The coating thermal diffusivity, measured at atmospheric pressure, varied from 0.015 at 20°C to 0.025 $\text{mm}^2\cdot\text{s}^{-1}$ at 250 °C. Such values are 10 times lower than the thermal diffusivity of YSZ coatings with a dual architecture with nanometer- and micrometer- sized features manufactured by air plasma spraying of micrometer-sized agglomerates made of nanometer-sized particles *Lima and Marple (2007)*.

For suspension plasma-sprayed YSZ TBCs *Vassen et al (2009)* showed that when applying the optimum process parameters for turbine components, homogeneous microstructures with an evenly distributed pore network could be obtained. Moreover, with appropriate spray conditions, coatings exhibited a high segmentation crack density (approximately 11 cracks. mm^{-1}) together with medium porosity (23%) (Figure 18a) and presented the best lifetimes in thermal cycling tests.

Gell *et al* (2008) studied the properties and resistance to thermal shock test of YSZ coatings made by solution precursor plasma spraying. They tested various atomization systems to inject the solution in the plasma jet. Figure 18b displays a YSZ coating manufactured with a conventional fluid atomizer that yielded a rather broad distribution of droplet sizes ($5 < d_p < 120 \mu\text{m}$) with a relatively large number of drops travelling in the plasma jet (Ar-H₂) fringes. The Vickers hardness of the coating was approximately 450 HV_{3N} and the porosity about 17 %. The vertical cracks were formed as a result of pyrolysis under heating of un-pyrolysed material imbedded within coating, thus resulting in shrinkage inducing tensile stresses. In Figure 18b dense regions of ultra-fine splats, small and uniformly dispersed voids and un-melted particles can be observed. During thermal cycling, the spallation life was improved by a factor of 2.5 compared with APS coatings on the same bond coat and substrate and by a factor of 1.5 compared with high-quality Electron Beam Physical Vapor Deposition (EB-PVD) coatings. The apparent thermal conductivity, as measured by the laser flash technique from 100 to 1000 °C, was about 1.0–1.2 W.m⁻¹.K⁻¹, a value lower than that of EB-PVD coatings, but higher than that of conventional air plasma-sprayed (APS) coatings.

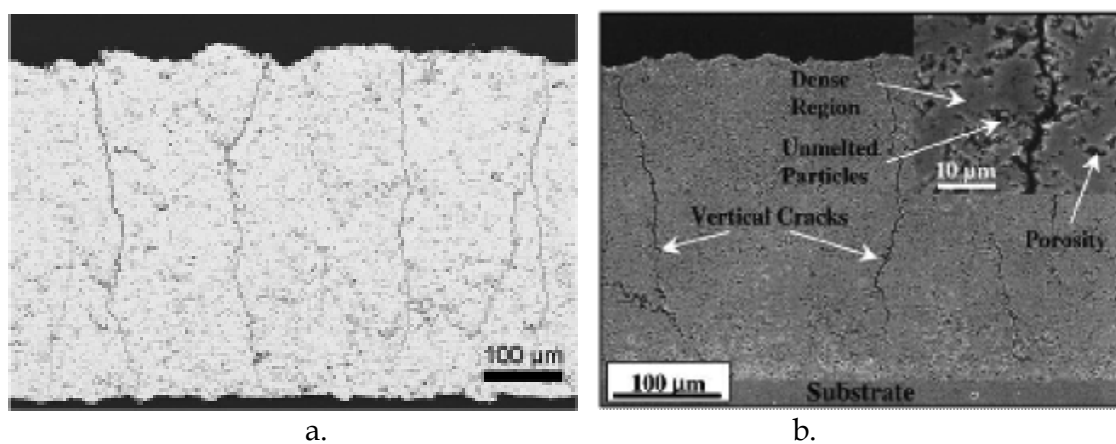


Fig. 18. (a) Suspension-plasma-sprayed TBC with medium porosity and high segmentation crack density Vassen *et al* (2009), (b) Features of solution plasma-sprayed TBCs using an air blast atomizer, details including vertical cracks, dense regions of ultra-fine splats, small and uniformly dispersed porosity, un-melted particles Gell *et al* (2008).

Another potential application of suspension plasma-sprayed YSZ coating is as a bond coat that provide for the adhesion of a YSZ conventional coating on smooth and thin (1 mm) super-alloy substrates that cannot be prepared by the usual grit blasting method. Vert *et al* (2010). First results seem promising.

7.2 Solid oxide fuel cells

A large body of studies has been devoted to solution and suspension coatings for solid oxide fuel cells (SOFCs). The objective was to produce the various components of the cell, anode, electrolyte and cathode, by using the same process. The tested coatings involved porous nickel-YSZ cermet coating for the anode, dense and thin (< 15 μm) YSZ coating for the electrolyte and porous perovskite, e.g. lanthanum ferro-cobaltite doped with strontium, (LSCF) or lanthanum manganite doped with strontium (LSM) for the cathode.

For the electrolyte *Brousse et al (2008)* have not succeeded to, but were close to, achieve suspension plasma-sprayed YPSZ coatings with a leakage below the value recommended for an impervious coating. *Jordan et al (2007)* have obtained reasonably dense YSZ coatings by using solution precursor plasma spraying with a specially designed capillary atomizer to atomize and inject the liquid feedstock in the plasma jet. *Marchand et al (2010)*, *Michaux et al (2010)*, *Wang et al (2010)* studied NiO-YSZ coating for the anode deposited by suspension and solution precursor plasma spraying and *Marchand et al (2007)* considered La_2NiO_4 suspension plasma-sprayed coatings for the cathode.

7.3 Wear resistant coatings

The materials tested for wear-resistant coatings are essentially alumina, alumina-titania, and alumina-YSZ. For suspension plasma sprayed alumina coatings *Darut et al (2010)* confirmed that the use of small particles in the suspension (down to $d_{50}=0.3 \mu\text{m}$) led to a low friction coefficient of about 0.2 against alumina. This coefficient could also be decreased by the addition of SiC in the Al_2O_3 matrix. The additive was not decomposed during suspension plasma spraying, while it is usually partially decomposed when sprayed as micrometer sized particles in conventional air plasma spraying. $\text{Al}_2\text{O}_3\text{-ZrO}_2$ composite coatings showed higher wear resistance than pure Al_2O_3 coatings, *Tingaud et al (2010)*.

Tarasi et al (2010) investigated the phase formation in $\text{Al}_2\text{O}_3\text{-YSZ}$ sprayed with an Axial III plasma torch. They found that the particle velocity was the key parameter to achieve stable or metastable phases. Stable phases came along with particle low velocity at impact while metastable phases with high particle velocity. *Darut et al (2009)* obtained dense and cohesive coatings of $\text{Al}_2\text{O}_3\text{-TiO}_2$. *Chen et al (2009)* have first produced an amorphous powder of $\text{Al}_2\text{O}_3\text{-ZrO}_2$, which was then dispersed in ethanol for suspension spraying. The resulting coating was composed of alpha Al_2O_3 and tetragonal ZrO_2 phases and showed a very homogeneous phase distribution compared to coatings sprayed with crystalline powder by suspension or conventional APS.

7.4 Bio-active coatings

Hydroxyapatite (HA) is a bioactive ceramic material with similar chemical composition and crystal structure to human bone. It is used as a coating material for the integration of prostheses into osseous tissue. *Jaworski et al (2010)* have recently presented the recent developments in suspension plasma sprayed HA coatings with coating thickness between 10 and 50 μm . Coatings phase analysis showed the presence of HA crystals and several phases due to the decomposition of HA during the treatment of HA particles in the plasma jet. These phases and their respective fractions are of great importance since they determine the biological behavior of the coating, such as its dissolution in vivo. *Huang et al (2010)* showed that solution spraying of HA led to lesser degree of decomposition during spraying. This was attributed to the evaporation of the water solvent, reducing the temperature during the process. Moreover coatings exhibited a higher content of OH⁻ groups, which may lead to a superior structural integrity.

7.5 Photo-catalytic coatings

TiO_2 coatings are used as photo-catalytic surfaces, to degrade organic pollutants but also as electron emitters for light-emitting devices *Jaworski et al (2010)*. The photo-catalytic

properties of TiO₂ depend on the phase composition of deposits. Anatase is generally assumed to present a higher photo-catalytic activity than rutile and authors generally consider that 65 vol. % of anatase is necessary to achieve an acceptable photo-catalytic performance. Furthermore, microstructural features such as porosity and specific surface are essential. *Toma et al (2010)* showed that plasma-sprayed suspensions contained up to 67 to 80 vol. % of anatase (most probably un-melted feedstock) for feedstock material containing about 80 vol. % of it.

Vaßen et al (2009) manufactured TiO₂ photovoltaic Graetzel cells by suspension plasma spraying using as feedstock anatase particles with a mean particle size of 60 nm. The coating was deposited on a cold substrate. Highly porous TiO₂ coatings with anatase contents of about 90% and crystallite sizes well below 50 nm were obtained. However, the photovoltaic cell design had still to be optimized to achieve sufficient efficiencies.

8. Conclusions

Plasma spray coatings from liquid feedstock have generated numerous new scientific articles and conference contributions, particularly during the last 6-7 years. All these works are based on results that emerged in the late-1990s making it possible to manufacture nanostructured thick (from about ten to hundred micrometers) coatings exhibiting numerous unique properties, such as good thermal insulation and resistance to thermal shock, excellent wear resistance and improved catalytic behavior. The two processes used are:

- i. Suspension thermal spraying with feedstock made of nanometer- or sub-micrometer-sized particles in suspension;
- ii. Liquid precursor thermal spraying with feedstock made of a solution.

Compared to conventional plasma spraying, solution and suspension spraying are by far more complex for the following reasons:

- To achieve a good control of drops or liquid jet penetration within the plasma jet they should have velocity and size distributions as narrow as possible, which is difficult to achieve, especially with atomization processes. Moreover liquid properties should be such that fragmentation could not take place in the plasma jet fringes.
- Liquid fragmentation depends strongly upon suspension and solution preparations. For suspensions solvent, dispersant, solid particles mass load, particles size distribution, particle manufacturing route, particles crystallographic state (crystallized or amorphous)... play a key role. For solutions the main parameters are the droplet size, the surface tension and boiling point of the liquid phase, the solute chemistry, its solubility and its mass diffusivity.
- The behavior of small particles generated into the plasma jet depends very much on their sizes. With nanometer-sized particles the Knudsen effect, increases drastically and their inertia is very low. Their initial velocity is thus very important for particles to hit the substrate (according to the Stokes effect) and depends on that of mother droplets. At last, with the thermophoresis effect, small particles are ejected from the hot gases jet as soon as they reach area where temperature gradients are very important.
- The heat transfer to the substrate can be very important due to spray distances that can be as short as 30 mm, resulting in heat fluxes up to 40 MW.m⁻² and must be controlled (cooling systems and spray pattern).

- The substrate roughness must be adapted to the size of the sprayed particles, which means that the roughness limit is around a ratio Ra/d_{50} below 2 to avoid stacking defects.
- At last it must be underlined that deposition efficiencies are lower (4 to 8 times) than those of conventional coatings.

Two problems are still pending: in-flight measurements and nano-structured coatings characterization.

In spite of them suspensions and solutions plasma sprayed coatings present new microstructures and often improved properties compared to conventional sprayed coatings. Possible applications are mainly in the field of energy conversion systems: TBCs, SOFCs, photo catalytic coatings, bioactive coatings and wear and corrosion resistant coatings. Further research works are needed to achieve a better understanding of phenomena controlling the deposit formation and properties before such coatings appear in commercial applications. This could/should require the development of new, dedicated plasma torches, with higher power to compensate for energy lost in liquid vaporization, and specifically adapted to the processing of liquids (more stable plasma flow, dedicated liquid injection systems and on-line control of liquid injection, safety issues...).

9. Nomenclature

d_l	liquid jet, drop or droplet diameter (m)
d_p	particle diameter (m)
l_{BL}	boundary layer thickness (m)
m_l	liquid mass flow rate ($kg \cdot s^{-1}$)
St	Stokes number ($St = (\rho_p \times d_p^2 \times v_p) / (\mu_g \times l_{BL})^{-1}$) (-)
u_r	relative velocity hot gases-liquid ($m \cdot s^{-1}$)
v_g	gas velocity ($m \cdot s^{-1}$)
v_l	liquid velocity ($m \cdot s^{-1}$)
v_p	particle velocity ($m \cdot s^{-1}$)
We	Weber number ($We = (\rho_g \times u_r^2 \times d_l) / \sigma_l$) (-)
Z	Ohnesorge number ($Z = \mu_l / (\rho_l \cdot d_l \cdot \sigma_l)^{0.5}$) (-)

Greek symbols

μ_l	Liquid viscosity (Pa.s)
ρ_g	Plasma specific mass ($kg \cdot m^{-3}$)
ρ_l	Liquid specific mass ($kg \cdot m^{-3}$)
σ_l	Liquid surface tension ($N \cdot m^{-1}$ or $J \cdot m^{-2}$)

Abbreviations

BL	boundary layer
d.c.	direct current
i.d.	internal diameter (m)
PIV	Particle Image Velocimetry
r.f.	radio frequency
SOFC	Solid Oxide Fuel Cell

SPTS	Solution Precursor Thermal Spraying
STS	Suspension Thermal Spraying
TBC	Thermal Barrier Coating
YPSZ	Yttria-Partially Stabilized Zirconia
YSZ	Yttria Stabilized Zirconia

10. References

- Bacciochini A., Montavon G., Ilavsky J., Denoirjean A. and Fauchais P., (2010), Porous architecture of SPS thick YSZ coatings structured at the nanometer scale (~50 nm), *J. Therm. Spray Technol.* 19, 198–206
- Bacciochini A., Ben-Ettouil F., Brousse E., Ilavsky J., Montavon G., Denoirjean A., Valette S. and Fauchais P. (2010) Quantification of void network architectures of as-sprayed and aged nanostructured yttria-stabilized zirconia (YSZ) deposits, *Surface and Coatings Technology* 205, 683–9
- Basu S., Jordan E.H. and Cetegen B.M., (2008), Fluidmechanics and heat transfer of liquid precursor droplets injected into high-temperature plasmas *J. Therm. Spray Technol.* 17 60–72
- Ben-Ettouil F., Denoirjean A., Grimaud A., Montavon G. and Fauchais P., (2009), Sub-micrometer-sized YSZ thermal barrier coatings manufactured by suspension plasma spraying: process, structure and some functional properties, in *Thermal Spray 2009: Proc. Int. Thermal Spray Conf. (Las Vegas, NV, USA)* (eds.) B. R. Marple et al (pub.) Materials Park, OH: ASM International) 193–9
- Bisson J.-F., Gauthier B. and Moreau C., (2003), Effect of plasma fluctuations on in-flight particle parameters *J. Therm. Spray Technol.* 12, 38–43
- Blazdell P. and Kuroda S., (2000), Plasma Spraying of Submicron Ceramic Suspensions Using a Continuous Ink Jet Printer, *Surface and Coatings Technology* 123(2-3) 239-246.
- Bouchard D., Sun L., Gitzhofer F., and Brisard G.M., (2006), Synthesis and Characterization of $\text{La}_{0.8}\text{Sr}_{0.2}\text{MO}_{3-\delta}$ (M = Mn, Fe, or Co) Cathode Materials by Induction Plasma Technology, *Journal of Thermal Spray Technology* 15(1) 37-45
- Boulos. M.I., Fauchais P., Vardelle A. and Pfender E., (1993), Fundamentals of Plasma Particle Momentum and Heat Transfer, in *Plasma Spraying Theory and Applications* (ed.) R. Suryanarayanan (pub.) World Scientific Singapore.
- Boulos M., Fauchais P. and Pfender E., (1994), *Thermal plasmas, Fundamentals and Applications* (pub.) Plenum Press NY and London
- Bouyer E., Gitzhofer F., and Boulos M.I., (1995), Suspension Plasma Spraying of Hydroxyapatite, *Proceedings of the 12 th International Symposium of Plasma Chemistry*, (ed.) J.V. Heberlein et al., (Minneapolis, MN: Organizing Committees of the 12th Int. Chem.,) 865-870,
- Bouyer E., Gitzhofer F., and Boulos M.I., (1997), The Suspension Plasma Spraying of Bioceramics by Induction Plasma, *JOM*, February 58-62
- Brousse E., Montavon G., Fauchais P., Denoirjean A., Rat V., Coudert J.-F. and Ageorges H., (2008), Thin and dense yttria-partially stabilized zirconia electrolytes for IT-SOFC manufactured by suspension plasma spraying, in *Thermal Spray Crossing Borders* (ed.) E. Lugscheider (pub.) DVS Düsseldorf, Germany, 547–52

- Caruyer C., Vincent S., Meillot E., Caltagirone J.-P., (2010), Modeling the first instant of the interaction between a liquid and a plasma jet with a compressible approach, *Surface & Coatings Technology* 205, 974–979
- Chandra S. and Fauchais P., (2009) Formation of solid splats during thermal spray deposition, *J. Therm. Spray Technol.* 18, 148–80
- Chen D., Jordan E. H. and Gell M., (2010), The solution precursor plasma spray coatings: influence of solvent type, *Plasma Chem. Plasma Process.* 30, 111–9
- Chen D., Jordan E.H., and Gell M., (2009) Suspension Plasma Sprayed Composite Coating Using Amorphous Powder Feedstock, *Appl. Surf. Sci.* 255(11) 5935-5938
- Chen D., E.H. Jordan and M. Gell, (2009) Microstructure of suspension plasma spray and air plasma spray Al_2O_3 - ZrO_2 composite coatings, *J. Therm. Spray Technol.* 18, 421–6
- Chen D., Jordan E. H. and Gell M., (2008), Effect of solution concentration on splat formation and coating microstructure using the solution precursor plasma spray process, *Surf. Coat. Technol.* 202, 2132–8
- Chen D., Jordan E. and Gell M., (2007), Thermal and crystallization behavior of zirconia precursor used in the solution precursor plasma spray process, *J. Mater. Sci.* 42, 5576–80
- Coudert J-F, Rat V. and Rigot D., (2007), Influence of Helmholtz oscillations on arc voltage fluctuations in a dc plasma spraying torch, *J. Phys. D: Appl. Phys.* 40, 7357–66
- Darut G., Ben-Ettouil F., Denoirjean A., Montavon G., Ageorges H., and Fauchais P., (2010), Dry Sliding Behavior of Sub- Micrometer-Sized Suspension Plasma Sprayed Ceramic Oxide Coatings, *J. Therm. Spray Technol.* , 19(1-2) 275-285
- Darut G., Valette S., Montavon G., Ageorges H., Denoirjean A., Fauchais P., Klyatskina E., Segova F., (2010) and Salvador M. D., Comparison of Al_2O_3 and Al_2O_3 - TiO_2 Coatings Manufactured by Aqueous and Alcoholic Suspension Plasma Spraying, in *Thermal Spray: Global Solutions for Future Application*, Singapore (2010), (pub.) DVS, Düsseldorf, Germany, 212-217
- Darut G., Ageorges H., Denoirjean A., Montavon G. and Fauchais P., (2009) Dry sliding behavior of sub-micrometer-sized suspension plasma sprayed ceramic oxide coatings, *J. Therm. Spray Technol.* 19, 275–85
- Davis J.R. (ed.), (2004), *Handbook of thermal spray technology*, Pub. ASM International, Materials Park, OH, USA, 338 pages
- Delbos C., Fazilleau J., Rat V., Coudert J.-F., Fauchais P. and Pateyron B., (2006) Phenomena involved in suspension plasma spraying: II, *Plasma Chem. Plasma Process.* 26, 393–414
- Etchart-Salas R., (2007), Direct current plasma spraying of suspensions of sub-micrometer sized particles. Analytical and experimental approach on phenomenon controlling coatings reproducibility and quality PhD Thesis University of Limoges (in French)
- Etchart-Salas R., Rat V., Coudert J.-F., Fauchais P., Caron N., Wittman K., Alexandre S., (2007), Influence of plasma instabilities in ceramic suspension plasma spraying, *Journal of Thermal Spray Technology*, 16(5-6) 857-865
- Fauchais P., (2004), Understanding plasma spraying: an invited review, *Journal of Physics D: Applied Physics*, 37, R86-R108
- Fauchais P., Etchart-Salas R., Rat V., Coudert J.-F., Caron N., Wittmann-Ténéze K., (2008) Parameters controlling liquid plasma spraying: solutions, sols, or suspensions, *Journal of Thermal Spray Technology*, 17(1) 31-59

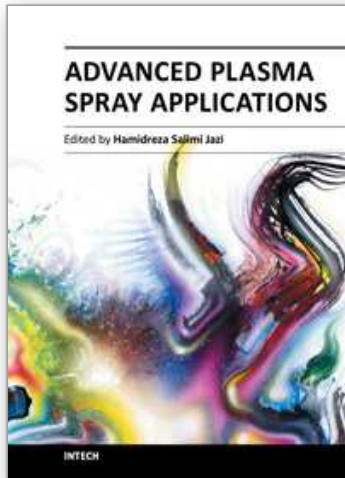
- Fauchais P., Montavon G., Lima R. and Marple B., (2011), Engineering a new class of thermal spray nano-based microstructures from agglomerated nanostructured particles, suspensions and solutions: an invited review, *Journal of Physics D: Applied Physics* 44, 093001 (53p)
- Fauchais P. and Vardelle A., (2011), Innovative and emerging processes in plasma spraying: from micro- to nano-structured coatings, *J. Phys. D: Appl. Phys* 44,
- Fazilleau J., Delbos C., Rat V., Coudert J. F., Fauchais P., Pateyron B., (2006) Phenomena involved in suspension plasma spraying part 1, *Plasma Chemistry Plasma Processes*, 26, 371-391
- Filkova I. and Cedik P., (1984), Nozzle Atomization in Spray Drying, *Advances Drying*, A.S. Mujumdar, Ed., Hemisphere Pub. Corp., 3 181-215
- Gell M., (1995), Application opportunities for nanostructured materials and coatings, *Materials Science Engineering*, 204(1) 246-251
- Gell M., Jordan E.H., Teicholz M., Cetegen B. M., Padture N., Xie L., Chen D., Ma X. and Roth J., (2008) Thermal barrier coatings made by the solution precursor plasma spray process *J. Therm. Spray Technol.* 17, 124-35
- Hammouda B., (2008) *The SANS Toolbox* (Gaithersburg, MD: Center for Neutron Research, National Institute of Standards and Technology) 657p
- Hermanek, F.J., *Thermal Spray Terminology and Company Origins*. (2001) ASM International, Materials Park, Ohio.
- Huang Y., Song L., Huang T., Liu X., Xiao Y., Wu Y., Wu F., and Gu Z., (2010), Characterization and Formation Mechanism of Nano- Structured Hydroxyapatite Coatings Deposited by the Liquid Precursor Plasma Spraying Process, *Biomed. Mater.* 5, 054113-120
- Ilavsky J., Jemian P. R., Allen A. J., Zhang F., Levine L. E. and Long G. G., (2009) Ultra-small-angle X-ray scattering at the advanced photon source, *J. Appl. Crystallogr.* 42, 1-11
- Jaworski R., Pawlowski L., Pierlot C., Roudet F., Kozerski S., and Petit F., (2010), Recent Developments in Suspension Plasma Sprayed Titanium Oxide and Hydroxyapatite Coatings, *J. Therm. Spray Technol.* 19(1-2) 240-247
- Jia L. and Gitzhofer F. (2010), Induction Plasma Synthesis of Nano-Structured SOFCs Electrolyte Using Solution and Suspension Plasma Spraying: A Comparative Study, *Journal of Thermal Spray Technology* 19(3) 566-574
- Jordan E.H., Gell M., Bonzani P., Chen D., Basu S., Cetegen B., Wu F., and Ma X. (2007), Making Dense Coatings with the Solution Precursor Plasma Spray Process, *Thermal Spray 2007: Global Coating Solution*, B.R. Marple, M.M. Hyland, Y.-C. Lau, C.-J. Li, R.S. Lima, and G. Montavon, Eds.), ASM International Materials Park, OH, USA 463-470, e-proceedings
- Killinger A., Gadow R., Mauer G., Guignard A., Vaßen R., and Stöver D., (2011) Review of New Developments in Suspension and Solution Precursor Thermal Spray Processes, *Journal of Thermal Spray Technology* 20(4) 677-695
- Landes K., (2006) Diagnostics in Plasma Spraying Techniques, *Surf. Coat. Technol.*, 201, 1948-1954
- Lee C.S. and Reitz R.D. (2001), Effect of liquid properties on the break-up mechanism of high-speed liquid drops *Atomization Sprays* 11, 1-18
- Lefebvre A.H., (1989), *Atomizations and Sprays*, Hemisphere Pub. Corp.

- Lima R. S. and Marple B.R. (2007) Thermal spray coatings engineered from nano-structured ceramic agglomerated powders for structural, thermal barrier and biomedical applications: a review, *Journal of Thermal Spray Technology* 16, 40-63
- Marchand O., Bertrand P., Mouglin J., Comminges C., Planche M.-P., Bertrand G., (2010) Characterization of suspension plasma-sprayed solid oxide fuel cell electrodes, *Surface & Coatings Technology* 205 993-998
- Marchand C., Vardelle A., Mariaux G., Lefort P., (2008), Modelling of the plasma spray process with liquid feedstock injection, *Surface and Coatings Technology*, 202, 4458-4464
- Mauer G., Guignard A., Vaßen R., Stöver D., (2010), Process diagnostics in suspension plasma spraying, *Surface & Coatings Technology* 205 961-966
- Michaux P., Montavon G., Grimaud A., Denoirjean A., and Fauchais P., (2010) Elaboration of Porous NiO/8YSZ Layers by Several SPS and SPPS Routes, *J. Therm. Spray Technol.*, 19(1-2) 317-327
- Oberste-Berghaus J., Legoux J.-G., and Moreau C., (2005) Injection Conditions and In-Flight Particle States in Suspension Plasma Spraying of Alumina and Zirconia Nanoceramics, ITSC 2005 (Düsseldorf, Germany), DVS e-proceedings
- Oberste Berghaus J., Bouaricha S., Legoux J.-G. and Moreau C., (2005), Suspension plasma spraying of nanoceramics using an axial injection torch, in *Thermal Spray Connects: Explore Its Surfacing Potential* (eds.) E. Lugscheider and C. C. Berndt (Düsseldorf, Germany: DVS-Verlag) e-proceedings
- Oberste-Berghaus J., Marple B. and Moreau C., (2006), Suspension plasma spraying of nanostructured WC-12Co coatings, *J. Therm. Spray Technol.* 15, 676-81
- Ozturk A. and Cetegen B. M., (2005), Modeling of axially and transversely injected precursor droplets into a plasma environment, *Int. J. Heat Mass Transfers* 48, 4367-83
- Ozturk A. and Cetegen B. M., (2006), Modeling of axial injection of ceramic, *Mater. Sci. Eng. A* 422, 163-75
- Pawlowski L., (2008), Finely grained nanometric and submicrometric coatings by thermal spraying: a review, *Surface and Coatings Technology*, 202(18), 4318-4328
- Portinha A., Teixeira V., Carneiro J., Martins J., Costa M. F., Vassen R. and Stöver D., (2005), Characterization of thermal barrier coatings with a gradient in porosity *Surf. Coat. Technol.* 195, 245-51
- Rampon R., Filiatre C. and Bertrand G., (2008), Suspension plasma spraying of YSZ coatings: suspension atomization and injection, *J. Therm. Spray Technol.* 17, 105-14
- Rampon P., Filiatre C., and Bertrand G., (2008), Suspension Plasma Spraying of YPSZ Coatings for SOFC: Suspension Atomization and Injection, *J. Therm. Spray Technol.*, 17(1), 105-114
- Ravi B.G., Sampath S., Gambino R., Devi P. S. and. Parise J.B, (2006), Plasma spray synthesis from precursors: progress, issues and considerations, *J. Therm. Spray Technol.* 15, 701-7
- Rice R. W., (1996), Porosity dependence of physical properties of materials: a summary review, *Key Eng. Mater.* 115, 1-19
- Saha A., Seal S., Cetegen B., Jordan E., Ozturk A. and Basu S., (2009), Thermo-physical processes in cerium nitrate precursor droplets injected into high temperature plasma *Surf. Coat. Technol.* 203 2081-91

- Schiller G., Müller M., and Gitzhofer F., (1999), Preparation of Perovskite Powders and Coatings by Radio Frequency Suspension Plasma Spraying, *Journal of Thermal Spray Technology* 8(3), 389-398
- Shan Y., Coyle T.W., and Mostaghimi J., (2010), Modeling the Influence of Injection Modes on the Evolution of Solution Sprays in a Plasma Jet, *Journal of Thermal Spray Technology* 19(1-2) 248-254
- Shan Y., Coyle T. W. and Mostaghimi J., (2007) Numerical simulation of droplet break-up and collision in solution precursor plasma spraying *J. Therm. Spray Technol.* 16 698-704
- Shen Y., Almeida V. A. B., and Gitzhofer F., (2011), Preparation of Nano-composite GDC/LSCF Cathode Material for IT-SOFC by Induction Plasma Spraying, *Journal of Thermal Spray Technology* 20(1-2), 145-153
- Singh N., Manshian B., Jenkins G.J.S., Griffiths S.M., Williams P. M., Maffei T. G. G., Wright, C. J., and Doak S. H., (2009) *Biomaterials* 30, 3891-914
- Tarasi F., Medraj M., Dolatabadi A., Oberste-Berghaus J., and Moreau C., (2010), Phase Formation and Transformation in Alumina/YSZ Nanocomposite Coating Deposited by Suspension Plasma Spray Process, *J. Therm. Spray Technol.* 19(4) 787-795
- Tingaud O., Bertrand P., and Bertrand G., (2010), Microstructure and Tribological Behavior of Suspension Plasma Sprayed Al₂O₃ and Al₂O₃-YSZ Composite Coatings, *Surf. Coat. Technol.* 205(4) 1004-1008
- Tingaud O., Grimaud A., Denoirjean A., Montavon G., Rat V., Coudert J.-F., Fauchais P. and Chartier T., (2008), Suspension plasma-sprayed alumina coating structures: operating parameters versus coating architecture *J. Therm. Spray Technol.* 17, 662-70
- Toma F.-L., Berger L.-M., Stahr C.C., Naumann T., and Langner S., (2010) Microstructures and Functional Properties of Suspension-Sprayed Al₂O₃ and TiO₂ Coatings: An Overview, *J. Therm. Spray Technol.* 19(1-2) 262-274
- Vaßen R., Stuke A., and Stöver D., (2009), Recent Developments in the Field of Thermal Barrier Coatings, *J. Therm. Spray Technol.* 18(2), 181-186
- Vaßen R., Kaßner H., Mauer G., and Stöver D., (2010) Suspension Plasma Spraying: Process Characteristics and Applications, *Journal of Thermal Spray Technology* 19(1-2) 219-225
- Vaßen R., Yi Z., Kaßner H., and Stöver D., (2009), Suspension Plasma Spraying of TiO₂ for the Manufacture of Photovoltaic Cells, *Surf. Coat. Technol.* 203(15) 2146-2149
- Viswanathan V., Laha T., Balani K., Agarwal A., Seal S., (2006), Challenges and Advances in Nanocomposite Processing Techniques, *Mat. Sc. and Eng.*, R54, 121-285
- Wang Y., Legoux J.-G., Neagu R., Hui R., Maric R., and Marple B. R., (2010), Deposition of NiO/YSZ Composite and YSZ by Suspension Plasma Spray on Porous Metal, in *Thermal Spray: Global Solutions for Future Application*, 2010 Singapore (pub.) DVS-Berichte, Düsseldorf, Germany, p 446-453
- Vert R., Chicot D., Dublanche-Tixier C., Meillot E., Vardelle A., and Mariaux G., (2010), Adhesion of YSZ Suspension Plasma -Sprayed Coating on Smooth and Thin Substrates, *Surf. Coat. Technol.* 205(4) 999-1003

- Wittmann-Ténèze K., Vallé K., Bianchi L., Belleville P. and Caron N., (2008), Nanostructured zirconia coatings processed by PROSOL deposition, *Surf. Coat. Technol.* 202, 4349-54
- Xie L., Ma X., Jordan E. H., Padture N. P., Xiao D. T. and Gell M., (2004), Deposition mechanisms of thermal barrier coatings in the solution precursor plasma spray process, *Surf. Coat. Technol.* 177-178, 103-7
- Xiong H.-B. and Lin J.-Z, (2009), Nano particles modeling in axially injection suspension plasma spray of zirconia and alumina ceramics, *J. Therm. Spray Technol.* 18(4), 887-95

IntechOpen



Advanced Plasma Spray Applications

Edited by Dr. Hamid Jazi

ISBN 978-953-51-0349-3

Hard cover, 250 pages

Publisher InTech

Published online 21, March, 2012

Published in print edition March, 2012

Recently, plasma spray has been received a large number of attentions for various type of applications due to the nature of the plasma plume and deposition structure. The plasma gas generated by the arc, consists of free electrons, ionized atoms, some neutral atoms, and undissociated diatomic molecules. The temperature of the core of the plasma jet may exceed up to 30,000 K. Gas velocity in the plasma spray torch can be varied from subsonic to supersonic using converging-diverging nozzles. Heat transfer in the plasma jet is primarily the result of the recombination of the ions and re-association of atoms in diatomic gases on the powder surfaces and absorption of radiation. Taking advantages of the plasma plume atmosphere, plasma spray can be used for surface modification and treatment, especially for activation of polymer surfaces. In addition, plasma spray can be used to deposit nanostructures as well as advanced coating structures for new applications in wear and corrosion resistance. Some state-of-the-art studies of advanced applications of plasma spraying such as nanostructure coatings, surface modifications, biomaterial deposition, and anti wear and corrosion coatings are presented in this book.

How to reference

In order to correctly reference this scholarly work, feel free to copy and paste the following:

P. Fauchais and A. Vardelle (2012). Solution and Suspension Plasma Spraying of Nanostructure Coatings, *Advanced Plasma Spray Applications*, Dr. Hamid Jazi (Ed.), ISBN: 978-953-51-0349-3, InTech, Available from: <http://www.intechopen.com/books/advanced-plasma-spray-applications/solution-and-suspension-plasma-spraying-of-nanostructure-coatings>

INTECH
open science | open minds

InTech Europe

University Campus STeP Ri
Slavka Krautzeka 83/A
51000 Rijeka, Croatia
Phone: +385 (51) 770 447
Fax: +385 (51) 686 166
www.intechopen.com

InTech China

Unit 405, Office Block, Hotel Equatorial Shanghai
No.65, Yan An Road (West), Shanghai, 200040, China
中国上海市延安西路65号上海国际贵都大饭店办公楼405单元
Phone: +86-21-62489820
Fax: +86-21-62489821

© 2012 The Author(s). Licensee IntechOpen. This is an open access article distributed under the terms of the [Creative Commons Attribution 3.0 License](#), which permits unrestricted use, distribution, and reproduction in any medium, provided the original work is properly cited.

IntechOpen

IntechOpen